A New Hybrid Finite-Volume/Particle Method for the PDF Equations of Turbulent Reactive Flows and Performance of Velocity Models

by

Özkan Eren

A Thesis Submitted to the
Graduate School of Engineering
in Partial Fulfillment of the Requirements for
the Degree of

Master of Science

in

Computational Science and Engineering

Koç University

June, 2006

Koç University

Graduate School of Sciences and Engineering

This is to certify that I have examined this copy of a master's thesis by

Özkan Eren

and have found that it is complete and satisfactory in all respects,
and that any and all revisions required by the final
examining committee have been made.

Committee Members:

_____

Assistant Prof. Metin Muradoğlu (Advisor)

_____

Assistant Prof. Mehmet Sayar

_____

Assistant Prof. Murat Sözer

Date: _____

To my Family

ABSTRACT

The consistent hybrid solution method has been recently developed and shown to be superior to the best alternative approach by as much as a factor of 50 or more, making the PDF methodology a feasible design tool in practical applications . In the present study, the hybrid solution method is improved significantly by replacing the density-based finite-volume (FV) solver with a SIMPLE type pressure-based FV solver of Peric (1999) and the new solution algorithm is used to simulate the bluff-body stabilized turbulent non-reacting and reacting flows studied experimentally by Dally et al. (1998). In the PDF methods, the transport equation for mass-weighted joint PDF is directly derived from the Navier-Stokes equations and the unclosed terms are modeled through construction of stochastic differential equations (SDEs). The closure is usually guided by existent Reynolds stress models such that the joint PDF model is equivalent to the corresponding Reynolds stress model at the second moment level. Although there exist advanced velocity models, the simplified Langevin model (SLM) has been usually used in the PDF computations due to its simplicity. In the present study, in addition to the SLM, we also consider two other popular velocity models, namely Lagrangian Isotropization of Production Model (LIPM) and Lagrangian Speziale Sarkar Gatski Model (LSSG) and evaluated their performances for the bluff-body flows. Since the focus of the present work is on the accurate calculations of mean and rms velocity fields, a simple flamelet chemistry model is employed to facilitate extensive numerical simulations. However, sensitivity of the computed results to the model constants for the mixture fraction and variance of the mixture fraction are also presented. An attempt is also made to optimize the LIPM and LSSG velocity models based on the bluff-body flows and significant improvement is achieved in predicting the mean fields for non-reacting case.

ÖZET

ssssssssssssssssssssssssssssssssssssSSSSSSSSSSSSSSSSSSSSSSSS

ACKNOWLEDGMENTS

I would like to thank, first and foremost, my advisor, Assistant Prof. Metin Muradoğlu for his guidance and support throughout my graduate study and during the completion of this thesis. I am extremely grateful to, Assistant Prof. Murat Sözer and Assistant Prof. Mehmet Sayar, for their participation in my thesis committee and for the critical reading of my thesis.

Also, I would like to thank all my friends at Koç University who made the two years an enjoyable period of time; my research group friends ; my grad student friends and all the people who surrounded me all the time especially Besray.

Last, I would like to thank my parents Zehra Eren, Cavit Eren for their love, affection and support throughout my life, without their encouragement I wouldn't be what I am today. I am very fortunate to be a part of such an affectionate family.

TABLE OF CONTENTS

LIST OF TABLES

LIST OF FIGURES

NOMENCLATURE

RANS	Reynolds Averaged Navier Stokes
FV	Finite Volume
g_z	gravitational acceleration
p	pressure
PDF	Probability Density Function
r and z	radial and axial coordinates
R_j	radius of the jet region
Re	Reynolds number
D_b	diameter of bluff-body
R_b	radius of bluff-body
ρ	density
t	physical time
U	velocity scale
u_x and u_y	velocity components in x and y coordinate directions

Chapter 1

INTRODUCTION

Most of the industrial and natural flows are turbulent and many involve chemical reactions. However the turbulence is still one of the major unsolved problems of classical physics. Although the Navier-Stokes equations are known to be the correct mathematical model for turbulent flows, the direct numerical simulation (DNS) is still limited to simple flows with low or moderate Reynolds numbers due to rapidly increasing computational cost with Reynolds number. In probability density function (PDF) methods, turbulent flows are modeled through modeled transport equation of a one-point, one-time PDF of selected flow properties. Compared to the traditional turbulence models PDF methods have a distinct advantage of being able to treat the important processes of convection and non-linear chemistry exactly without any modeling assumptions. In addition, the effects of the mean pressure gradient and the body forces also appear to be in closed form and only fluctuating pressure gradient and molecular transport terms need to be modeled. The unclosed terms are closed through construction of stochastic differential equations that represent the same PDF as the turbulent flows [21].

As for any turbulence model, an efficient numerical solution algorithm is of crucial importance in the PDF methods. A significant progress has been recently made in this direction by the development of the consistent hybrid finite-volume (FV)/particle-based Monte Carlo method [11, 16, 18]. It has been shown that the consistent hybrid method is upto 100 times more efficient than the best available alternative solution algorithm of the self-contained particle-mesh method implemented in *pdf2dv* code [23]. The major advantage of the hybrid method comes from the fact that it is designed to combine the best features of the FV and particle methods and to avoid their deficiencies when used alone. It has been shown that it virtually eliminates the bias error and significantly reduces the statistical noise in mean fields [11, 16]. In addition, the hybrid method can be easily coupled with existing

flow solvers including the commercial CFD packages. In the hybrid method, a finite-volume solver is used to solve the mean mass, momentum and energy conservation equations while a particle-based Monte-Carlo algorithm is employed to solve the transport equation of the joint PDF of the fluctuating velocity, turbulent frequency and compositions. The method is fully consistent at the level of the equations since all the equations solved by the hybrid method are directly derived from the modeled joint PDF transport equation. In addition, a full consistency at the numerical level is achieved by the correction algorithms developed by Muradoglu et al. [18]. Although the consistent hybrid method coupled with the correction algorithms has been successfully applied to various turbulent flames [4, 10, 13, 15, 17], its main deficiency was the lack of robustness and the extreme sensitivity to the relaxation parameters [10]. In particular, the previous versions of the hybrid algorithm failed to achieve a grid convergence for the non-reacting bluff-body flow [10]. When the grid is refined more than a threshold, both the loosely-coupled [16] and tightly-coupled [11] hybrid solvers resulted in a vortex shedding that has not been observed experimentally [6] and it was not clear whether this unphysical behavior was due to the models used or due to the numerical solution algorithms. The primary purpose of the present thesis is to resolve this problem and to develop an accurate and robust consistent hybrid algorithm for solving the PDF equations of turbulent reacting flows and to apply the new solver to assess the performance of the most widely used velocity models. For this purpose, the density-based FV method used in the previous version of the loosely-coupled hybrid algorithm [16] is replaced with a pressure-based SIMPLE type FV solver [20] since there was some evidence that the lack of robustness of the old version of the hybrid method was due to the excessive numerical dissipation needed to maintain the numerical stability of the FV algorithm. In addition to this, turbulent combustion usually takes place at low Mach numbers in order to avoid rapid and large increase in pressure during the heat addition and the pressure-based solvers have been designed and proven to be efficient in such flow regimes [20]. Note that the FV algorithm used in this study belongs to the class of flow solvers that are used in virtually all the commercial CFD packages including Star-CD [1], Fluent [2] and CFX [3]. It is found that the new hybrid algorithm is more robust than the old version and does not produce any unphysical vortex shedding when applied to the non-reacting bluff-body flow while retaining all the advantages of the consistent hybrid method. In this new version of

the hybrid algorithm, the energy conservation equation is not solved and the mean density field is directly supplied by the particle method to the FV solver. It is found that the noisy density field extracted from the particles does not cause any significant stability problem as long as it is time averaged over a sufficiently long time scale.

The new hybrid method is also used to assess the performance of the velocity models including the simplified Langevin model (SLM), the Lagrangian isotropization of the production model (LIPM) and the Lagrangian Speziale-Sarkar-Gatski model (LSSG). For this purpose, non-reacting and reacting bluff-body flows are selected as test cases and the computational results are compared with the experimental data [6]. In addition, sensitivity of the computational results to the model coefficients are examined and an attempt is made to optimize the model constants.

The thesis is organized into four main parts. In the next chapter, the PDF method is briefly reviewed and the model equations are described. The numerical solution algorithm is discussed in Chapter 3. In this chapter, the hybrid algorithms are briefly reviewed and the present version is described in details. The accuracy and robustness of the present hybrid method are demonstrated using the non-reacting and reacting bluff-body flows. Then the method is used to study the performance of the velocity models in Chapter 4. Finally some conclusions are drawn in Chapter 5.

Chapter 2

JOINT PDF MODELING OF TURBULENT REACTIVE FLOWS

The joint PDF method is briefly reviewed and the model equations are described in this chapter. The joint probability density function (PDF) method has proven to be a successful approach for modeling turbulent reacting flows [21]. In PDF methods, turbulence closure is achieved through a modeled transport equation for the one-point, one-time PDF of selected flow properties. In this approach the convection and non-linear chemical reactions are represented exactly without modeling assumptions–capability not possible by any other approaches. In addition, body forces and the mean pressure gradient also appear in closed form, but the fluctuating pressure gradient and molecular transport terms need to be modeled. In particular, the exact treatment of the non-linear chemical reactions makes the PDF method very attractive for computations of turbulent reacting flows. It has been shown that the PDF approach is very successful to correctly resolve the important processes of local extinction and reignition [28, 30].

2.1 Joint PDF Formulation

The one-point, one-time, mass-weighted joint PDF of velocity $\boldsymbol{U}$ =$(\mathrm{U}_1, \mathrm{U}_2, \mathrm{U}_3)$ and compositions $\boldsymbol{\phi} = (\phi_1, \phi_2, ..., \phi_{n\phi})$ at location $\mathbf{x}$ and time t is defined as

$$\langle\rho\rangle\, \tilde{f}'(\boldsymbol{V},\boldsymbol{\psi};\boldsymbol{x},t) \equiv \rho(\boldsymbol{\psi})\, \langle\delta(\boldsymbol{V}-\boldsymbol{U})\delta(\boldsymbol{\psi}-\boldsymbol{\phi})\rangle\,, \tag{2.1}$$

where ρ is the density, $\boldsymbol{V}$ =$(\mathrm{V}_1, \mathrm{V}_2, \mathrm{V}_3)$ and $\boldsymbol{\psi} = (\psi_1, \psi_2, ..., \psi_{n\psi})$ are the sample space variables for velocity $\boldsymbol{U}$ and the compositions $\boldsymbol{\psi}$, respectively. The transport equation for $\tilde{f}'(\boldsymbol{V},\boldsymbol{\psi};\boldsymbol{x},\mathrm{t})$ can be derived from the Navier-Stokes equations using the standard techniques [21] and is given by

$$\begin{aligned}\frac{\partial \langle\rho\rangle \tilde{f}^{'}}{\partial t} &+ V_j \frac{\partial \langle\rho\rangle \tilde{f}^{'}}{\partial x_j} - \frac{\partial \langle p\rangle}{\partial x_j}\frac{\partial \tilde{f}^{'}}{\partial V_j} + \frac{\partial}{\partial \psi_\alpha}(\langle\rho\rangle S_\alpha \tilde{f}^{'}) \\ &= \frac{\partial}{\partial V_j}\left(\left\langle -\frac{\partial \tau_{ij}}{\partial x_i} + \frac{\partial p^{'}}{\partial x_j} | \boldsymbol{V},\boldsymbol{\psi} \right\rangle \tilde{f}^{'}\right) + \frac{\partial}{\partial \psi_\alpha}\left(\left\langle \frac{\partial J_i^\alpha}{\partial x_i} | \boldsymbol{V},\boldsymbol{\psi} \right\rangle \tilde{f}^{'}\right), \end{aligned} \tag{2.2}$$

where brackets with vertical bar $\langle ...|... \rangle$ stands for the conditional expectation. As can be seen in Eq. (2.2), $\tilde{f}'$ evolves in $(7+n_s)$ dimensional space for a three dimensional unsteady flow, where n_s is the number of species. All the terms on the left-hand side of Eq. (2.2) are in closed form and are treated exactly but the terms on the right hand side are not closed and need to be modeled. The unclosed terms represent the transport in the velocity space due to fluctuating pressure gradient $\frac{\partial p^{'}}{\partial x_j}$, the transport by the molecular viscous stresses τ_{ij} and transport in the composition space by the molecular diffusion J_i^α (of the scalar α in direction i). The unclosed terms are modeled through construction of stochastic differential equations as discussed below.

2.1.1 Velocity Model

Viscous dissipation and fluctuating pressure gradient are modeled through a velocity model and the Langevin models have been widely used in the PDF methods for this purpose [21, 24]. The most general form of the Langevin model can be written as [9]

$$dU_i(t) = -\frac{1}{\langle\rho\rangle}\frac{\partial\langle p\rangle}{\partial x_i} - G_{ij}\Omega\left(U_i - \tilde{U}_i(t)\right)dt + (C_0 k\Omega)^{1/2} dW_i, \tag{2.3}$$

where p is the pressure,

$$\Omega \equiv C_\Omega \frac{\langle\rho\omega|\omega \geq \tilde{\omega}\rangle}{\langle\rho\rangle}, \tag{2.4}$$

is the conditional Favre averaged turbulence frequency, and

$$k = \frac{1}{2}\widetilde{u_i u_i}, \tag{2.5}$$

is the turbulent kinetic energy. The fluctuating velocity is defined as $\mathbf{u} = \mathbf{U} - \tilde{\mathbf{U}}$, where $\tilde{\mathbf{U}}$ is the Favre averaged mean velocity. Diffusion in velocity space is represented as a three dimensional Wiener process $\mathbf{W}(t)$, where $dW_i(t) = W_i(t+dt) - W_i(t)$ is normally distributed with $\langle dW_i(t)\rangle = 0$ and $dW_i(t)dW_j(t) = dt\delta_{ij}$. In Eq. (2.3), the second order tensor G_{ij} is usually specified such that the corresponding PDF model becomes equivalent to a Reynolds

stress model at the second moment closure level [22, 24] and it can be written in the most general form as

$$G_{ij} \equiv \Omega(\alpha_1\delta_{ij} + \alpha_2 b_{ij} + \alpha_3 b_{ij}^2) + H_{ijkl}\frac{\partial \tilde{U}_k}{\partial x_l}, \tag{2.6}$$

where the fourth-order tensor $\mathbf{H}$ is

$$\begin{aligned} H_{ijkl} &= \beta_1\delta_{ij}\delta_{kl} + \beta_2\delta_{ik}\delta_{jl} + \beta_3\delta_{il}\delta_{jk} + \gamma_1\delta_{ij}\delta_{kl} \\ &+ \gamma_2\delta_{ik}b_{jl} + \gamma_3\delta_{il}b_{jk} + \gamma_4 b_{ij}\delta_{kl} + \gamma_5 b_{ik}\delta_{jl} \\ &+ \gamma_6 b_{il}\delta_{jk}, \end{aligned} \tag{2.7}$$

and the normalized anisotropy tensor is defined as

$$b_{ij} = \frac{\langle u_i u_j\rangle}{\langle u_k u_k\rangle} - \frac{1}{3}\delta_{ij}. \tag{2.8}$$

The terms in $\alpha_{(i)}$ are the most general expressions involving the Reynolds stress anisotropy b_{ij} alone, while the term in $\mathbf{H}$ is linear both in the mean velocity gradients and in the anisotropy [24]. The model coefficients are selected based on the corresponding Reynolds stress model at the second moment closure level as discussed by Pope [22, 24]. The three most widely used models are considered here and the coefficients are specified accordingly. These models are the simplified Langenvin model (SLM), Lagrangian IP model (LIPM) and the Lagrangian Speziale-Sarkar-Gatski model (LSSG). The coefficient α_1 is specified as

$$\alpha_1 = \begin{cases} -(\frac{1}{2} + \frac{3}{4}C_0 & \text{for} \quad SLM \\ -(\frac{1}{2} + \frac{3}{4}C_0) + 3\alpha_2 b_{ll}^3 + \frac{1}{2}C_2^{IPM}\frac{P}{k\Omega} & \text{for} \quad LIPM \\ -(\frac{1}{2} + \frac{3}{4}C_0) - \frac{1}{4}C_2^{SSG}b_{ll}^2 + (3\alpha_2 - \frac{3}{4}C_2^{SSG})b_{ll}^3 + \frac{3}{8}(C_3^{SSG} - C_{3*}^{SSG}b')\frac{P}{k\Omega} & \text{for} \quad \text{LSSG.} \end{cases} \tag{2.9}$$

The specifications of all the other coefficients corresponding to the SLM, LIPM and LSSG models are summarized in Tables 2.1 and 2.2. Note that the SLM model is equivalent to the Rotta's model [25] while the LIPM and LSSG models approximately correspond to the isotropization of production model (IPM) of Naot et al. [19] and the Speziale-Sarkar-Gatkski model [27] at the second moment closure level.

2.1.2 Turbulent Frequency Model

Turbulent frequency model provides a turbulence time scale needed to close the equations for the velocity and mixing models. The stochastic model for turbulent frequency is given

Constant	Value	Used in
C_0	2.1	SLM
C_Ω	0.6893	definition of Ω
$C_{\omega 1}$	0.65	turbulence frequency model
$C_{\omega 2}$	0.9	turbulence frequency model
C_3	1.0	turbulence frequency model
C_4	1.0	turbulence frequency model
C_ϕ	2.0	IEM mixing model

Table 2.1: Model Constants.

Coefficient	SLM	LIPM	LSSG
α_1	- $(\frac{1}{2}+\frac{3}{4}C_0)$	Eq. 2.9	Eq. 2.9
α_2	0	3.5	4.0-1.7$\frac{P}{\varepsilon}$
α_3	0	-3α_2	$\frac{3}{4}C_2^{SSG}-3\alpha_2$
β_1	0	-0.2	-0.2
β_2	0	$\frac{1}{2}(C_2^{IPM}+1)$	$\frac{3}{8}(C_3^{SSG}-C_3^{SSG}b')+0.5$
β_3	0	$\frac{1}{2}(C_2^{IPM}-1)$	$\frac{3}{8}(C_3^{SSG}-C_3^{SSG}b')-0.5$
$\gamma_{1,2,3,4}$	0	0	0
γ_5	0	$\frac{3}{2}(1-C_2^{IPM})$	$\frac{3}{2}-\frac{3}{4}C_5^{SSG}$
γ_6	0	-$\frac{3}{2}(1-C_2^{IPM})$	$-\frac{3}{2}+\frac{3}{4}C_5^{SSG}$
Constants	$C_0=2.1$	$C_0=2.1, C_2^{IPM}=0.6$	$C_0=2.1, C_2^{SSG}=4.2,$ $C_3^{SSG}=0.8, C_3^{SSG}=1.0$ $C_5^{SSG}=0.4$

Table 2.2: Velocity Model Constants.

by [26]

$$d\omega(t) = -C_3(\omega-\tilde{\omega})\Omega dt - S_\omega\Omega\omega(t)dt + (2C_3C_4\tilde{\omega}\Omega\omega(t))^{1/2}dW, \tag{2.10}$$

where W is an independent Wiener process, and the source term S_ω is defined as

$$S_\omega = C_{\omega 2} - C_{\omega 1}\frac{P}{k\Omega}, \tag{2.11}$$

where $C_{\omega 1}$, $C_{\omega 2}$, C_3, C_4 are model constants specified in Table 2.1.

2.1.3 Chemistry and Mixing Models

A simple flamelet model is used throughout this work in order to facilitate extensive computational simulations. In this model, the thermochemical state is characterized solely by the mixture fraction defined as

$$\xi = \frac{Z_i - Z_{i2}}{Z_{i1} - Z_{i2}}, \tag{2.12}$$

where the subscripts 1 and 2 denote the fuel and oxidizers, respectively, and Z_i is the mass fraction of the element i. Mixing models are needed to close the molecular diffusion terms in Eq.(2.2). There are several mixing models available but we use here the simplest one, the interaction by exchange with the mean (IEM) model [7]. In the IEM model, the compositions evolve by

$$d\phi(t) = -\frac{1}{2} C_\phi \Omega(\boldsymbol{\phi}(\mathrm{t}) - \tilde{\boldsymbol{\phi}}) dt, \tag{2.13}$$

where C_ϕ is the model constant specified in Table 2.1. Note that $\boldsymbol{\phi} = \xi$ in this study.

2.1.4 Modeled PDF evolution equation

The modeled mass-weighted JPDF of velocity, turbulent frequency, and compositions is defined as

$$\langle\rho\rangle \, \tilde{f}(\boldsymbol{V},\boldsymbol{\psi},\theta;\mathrm{x},\mathrm{t}) = \rho(\boldsymbol{\psi}) \left\langle \delta(\boldsymbol{U} - \boldsymbol{V}) \delta(\boldsymbol{\psi} - \boldsymbol{\phi}) \delta(\theta - \omega) \right\rangle . \tag{2.14}$$

The transport equation for $\tilde{f}(\boldsymbol{V},\boldsymbol{\psi},\theta;\boldsymbol{x},t)$ is derived from Eqs.(2.3), (2.10) and (2.13) and the advection equation $\frac{d\mathbf{X}}{dt} = \tilde{\boldsymbol{U}} + \mathbf{u}$ and is given by

$$\begin{aligned}
\frac{1}{\langle\rho\rangle} \frac{\partial(\langle\rho\rangle \, \tilde{f})}{\partial t} &= -\frac{V_i}{\langle\rho\rangle} \frac{\partial}{\partial x_i}(\langle\rho\rangle \, \tilde{f}) + \frac{\partial \langle\rho\rangle}{\partial x_i} \frac{\partial \tilde{f}}{\partial V_i} \\
&+ \Omega G_{ij} \frac{\partial}{\partial V_j}[\tilde{f}(V_i - \tilde{U}_i)] + \frac{1}{2} C_0 k \Omega \frac{\partial^2 \tilde{f}}{\partial V_i \partial V_i} \\
&+ \Omega \frac{\partial}{\partial \theta}(\tilde{f} \theta S_\omega) + C_3 \Omega \frac{\partial}{\partial \theta}[\tilde{f}(\theta - \tilde{\omega})] + C_3 C_4 \Omega \tilde{\omega} \frac{\partial^2}{\partial \theta^2}(\tilde{f}\theta) \\
&- \frac{\partial}{\partial \psi_\alpha}[\tilde{f} S_\alpha] + \frac{1}{2} C_\phi \Omega \frac{\partial}{\partial \psi_\alpha}[\tilde{f}(\psi_\alpha - \tilde{\phi}_\alpha)].
\end{aligned} \tag{2.15}$$

As can be seen in Eq. (2.15), $\tilde{f}$ evolves in a high dimensional space, e.g., for a 3D flow it evolves in $(8 + n_s)$ dimensional space, where n_s is the number of compositions. Therefore

it is infeasible to solve this equation using conventional numerical methods such as finite-difference or finite-volume methods since the computational cost increases exponentially with the dimension of the equation in these methods. The only remaining alternative is the Monte Carlo method in which the computational cost increases only linearly with the dimensions. Although there exist Eulerian implementations of the Monte Carlo method for the PDF equations, the preferred solution method is the Lagrangian particle method [24].

2.2 Equations Solved by the Hybrid Method

All the equations solved by the hybrid method are derived directly from modeled JPDF equation and are thus fully consistent at the level of equations. The equations solved by the FV method and particle method are briefly described here.

2.2.1 Mean Flow Equations Solved By the FV Method

In the present hybrid method, the FV solver is used to solve continuity and momentum equations. The mean mass conservation equation is obtained by integrating Eq.(2.15) over the entire sample space and is given by

$$\frac{\partial}{\partial t}\langle\rho\rangle + \frac{\partial}{\partial x_i}(\langle\rho\rangle \tilde{U}_i) = 0. \tag{2.16}$$

Similarly the mean momentum equations are obtained from Eq.(2.15) as the first moments of the velocity components and are given by

$$\frac{\partial}{\partial t}(\langle\rho\rangle \tilde{U}_i) + \frac{\partial}{\partial x_j}(\langle\rho\rangle \tilde{U}_i\tilde{U}_j + \langle p\rangle \delta_{ij}) = -\frac{\partial}{\partial x_j}(\langle\rho\rangle \widetilde{u_i u_j}) \tag{2.17}$$

Note that the Reynolds stress terms appearing in Eq. (2.17) are provided by the particle method. The mean density field is also extracted from the particles and is passed to the FV code as will be discussed in the next Chapter so that there is no need to solve for the mean energy conservation equation in the present hybrid method.

2.2.2 The Equations Solved By the Particle Algorithm

A particle based Monte Carlo method is used to solve the joint PDF transport equation of fluctuating velocity, turbulent frequency and compositions. The equations solved by the particle method are again derived directly from the modeled joint PDF evolution equation

in the same way as described by Muradoglu et al. [18] and are summarized here. A fluid particle moves with the local flow velocity, i.e.,

$$\frac{dX_i(t)}{dt} = \tilde{U}_i(t) + u_i(t). \tag{2.18}$$

The fluctuating velocity evolves by

$$du_i(t) = \frac{1}{\langle\rho\rangle}\frac{\partial\,\langle\rho\widetilde{u_i u_j}\rangle}{\partial x_j}dt - u_j\frac{\partial\tilde{U}_i}{\partial x_j}dt - G_{ij}\Omega u_j(t)dt + (C_0 k\Omega)^{1/2}dW_i. \tag{2.19}$$

Finally the turbulent frequency and the compositions evolve by Eqs.(2.10) and (2.13), respectively.

The FV and particle algorithms are used to solve their respective equations in a pseudo loosely-coupled fashion as discussed in the next chapter.

Chapter 3

NUMERICAL METHOD

The PDF model equations have been described in the previous chapter. In this chapter, the hybrid FV/particle method is presented. Firstly the FV and particle algorithms are described separately and then the coupled FV/particle method is discussed. Since the present hybrid method is essentially the same as that of Muradoglu et al.[18], the general methodology is briefly discussed for completeness and emphasis is placed on the FV solver and on the associated coupling issues. Finally the new hybrid algorithm is applied to the non-reacting and reacting bluff-body flows in order to demonstrate its numerical accuracy and robustness.

3.1 Finite-Volume Scheme

The FV algorithm is essentially based on the cell-centered finite-volume scheme implemented in *caffa* code [20]. The code has been downloaded from the Internet and adopted to solve the mean flow equations, i.e., Eqs.(2.16) and (2.17). The method is based on the SIMPLE algorithm[5] and is second order accurate in space. Although the FV solver has both the steady and unsteady versions, only the steady version is used in the present study. Note that the method is also second order accurate in time when it is used in the time-accurate mode. The FV method and the SIMPLE scheme are discussed below.

3.1.1 FV Method

The mean mass conservation and the Favre averaged Navier-Stokes equations can be integrated over the control volume *abcd* as sketched in Fig. 3.1 and, using the Stokes' theorem,

the mean flow equations can be expressed in the integral form as

$$\int_{abcd} \langle\rho\rangle \tilde{U}_i n_i dS = 0, \tag{3.1}$$

$$\frac{\partial}{\partial t}\int_{\Omega} \langle\rho\rangle \tilde{U}_i d\Omega + \int_{abcd} \langle\rho\rangle \tilde{U}_i \tilde{U}_j n_j dS = -\int_{abcd} \langle\rho\rangle \widetilde{u_i u_j} n_j dS - \int_{abcd} \langle p\rangle \delta_{ij} n_j dS, \tag{3.2}$$

where the viscous stress terms are neglected in the momentum equations and $\mathbf{n}$ denotes the normal vector. A typical collocated FV grid is shown in Fig. 3.1. The present FV scheme is fully implicit and the resulting equations are solved iteratively. The basic idea is explained here and details can be found in Peric [20]. The surface integrals are split into four control volume (CV) face integrals. Approximation of the convective and diffusive fluxes and the source terms are considered on east CV face denoted by e in the sketch in Fig. 3.1. The other faces are treated in a similar way and the results can be obtained by a simple index substitution. Second order central differences are adopted to approximate spatial derivatives. Fluxes are approximated such that the quantities at a CV face center represent the mean values over the face. On the m^{th} outer iteration, all the nonlinear terms are approximated by a product of an 'old' (from the preceding outer iteration) and a 'new' value. Thus, in discretizing the momentum equations, the mass flux through each CV face is evaluated using the existing velocity field and is assumed to be known, i.e.,

$$\dot{m}_e^m = \int_{abcd} \langle\rho\rangle \tilde{U}_i n_i dS \approx (\langle\rho\rangle \tilde{U}_e)_e^{m-1} S_e, \tag{3.3}$$

where S_e is the area of eastern face and U_e is the velocity component in the direction of normal vector. Note that, unless specified otherwise, all the quantities are written for the m^{th} outer iteration and the superscript m is dropped in the remainder of this section. Mass fluxes at the faces of the CVs are obtained by linear interpolations. For instance, the mass flux on the east CV face is calculated as

$$\dot{m}_e = \frac{1}{2}(\dot{m}_P + \dot{m}_E). \tag{3.4}$$

Mass fluxes at the other faces can be calculated by substituting corresponding indices. Similarly, the convective flux through e face is given by

$$\int_{abcd} \langle\rho\rangle \tilde{U}_i \tilde{U}_j n_j dS \approx (\dot{m}\tilde{U}_i S)_e. \tag{3.5}$$

The CV face value of $\tilde{U}_i$ used in the above expression can be found using simple linear interpolation *central difference scheme* (CDS), but some iterative solvers fail to converge when applied to algebraic equation systems derived from central difference approximations of convective fluxes because the matrices may not be diagonally dominant in this case. Thus these equations are solved using *deferred correction* approach [20] in which the flux is expressed as

$$F^c_{i,e} = \dot{m}_e \tilde{U}^{UDS}_{i,e} + \dot{m}_e (\tilde{U}^{CDS}_{i,e} - \tilde{U}^{UDS}_{i,e})^{m-1}, \tag{3.6}$$

where superscripts CDS and UDS denote approximations by central and upwind differences, respectively. The outward unit normal vector at CV face e is $\boldsymbol{i}$, and thus the turbulent fluxes are calculated as

$$Q^r_{i,e} = -\int_{abcd} \widetilde{u_i u_x} dS \approx (\widetilde{u_i u_x})_e S_e. \tag{3.7}$$

Finally the pressure terms are approximated as

$$Q^p_u = -\int_S p\boldsymbol{i} \cdot \boldsymbol{n} dS \approx -(p_E S_E - p_P S_P)^{m-1}. \tag{3.8}$$

The approximation to the complete momentum equation is then given by

$$F^c_i = Q^r_i + Q^p_i + Q^r_i, \tag{3.9}$$

Then the total fluxes for the CV is given by

$$F^c = F^c_e + F^c_w + F^c_n + F^c_s. \tag{3.10}$$

When the approximation for the convective fluxes are substituted into Eq. 3.9, an algebraic equation is obtained in the form

$$A^u_P \tilde{U}_{i,P} + \sum_l A^u_l \tilde{U}_{i,l} = Q^u_P, \quad l = E, W, N, S. \tag{3.11}$$

The coefficients depend on the approximations used, for instance, for the UDS approximations applied for convective fluxes, the coefficient for the convective flux on face e can be given by

$$A^u_E = min(\dot{m}^u_e, 0).$$

The corresponding coefficients for other faces can be obtained by changing the indices. Similarly

$$A^u_P = -\sum_l A^u_l, \quad l = E, W, N, S.$$

The source term Q_P^u contains the pressure and Reynolds stress terms as well as the portion of convective fluxes resulting from the deferred correction and is given by

$$Q_P^u = Q_u^p + Q_u^b + Q_u^c + Q_u^r, \tag{3.12}$$

where

$$Q_{\tilde{U}_i}^c = \left[(F_{\tilde{U}_i}^c)^{UDS} - (F_{\tilde{U}_i}^c)^{CDS} \right]^{m-1}. \tag{3.13}$$

The convective terms are calculated using the velocities from the previous outer iteration $m-1$. Note that solution for the above momentum equation yields a velocity field that does not satisfy the mass conservation. Therefore the mass conservation is enforced through pressure correction using the SIMPLE algorithm of Caretto et al. [5] as briefly discussed below.

3.1.2 SIMPLE Method

In this subsection, the axial and radial components of velocity $\tilde{U}_i$ are denoted by u and v, respectively, for simplicity. The linearized momentum equations, i.e., Eq. 3.11 are solved with sequential solution method [20] using the "*old*" mass fluxes and the pressure from the previous outer iteration. This produces new velocities u^* and v^* which do not necessarily satisfy the continuity equation. Thus we have

$$\dot{m}_e^* + \dot{m}_w^* + \dot{m}_n^* + \dot{m}_s^* = \Delta\dot{m}_P^*, \tag{3.14}$$

where $\Delta\dot{m}_P^*$ is the residual. The velocity components u^* and v^* calculated from the momentum equations can be expressed as

$$u_e^* = \tilde{u}_e^* - \frac{S_e}{A_P^u}(p_E - p_P)^{m-1}, \tag{3.15}$$

where $\tilde{u}_e^*$ is shorthanded notation for

$$u_e^* = \frac{Q_P^u - Q^p - \sum_l A_l^u u_l^*}{A_P}. \tag{3.16}$$

Analogously, v_n^* is expressed as

$$v_n^* = \tilde{v}_n^* - \frac{S_n}{A_P^v}(p_N - p_P)^{m-1}. \tag{3.17}$$

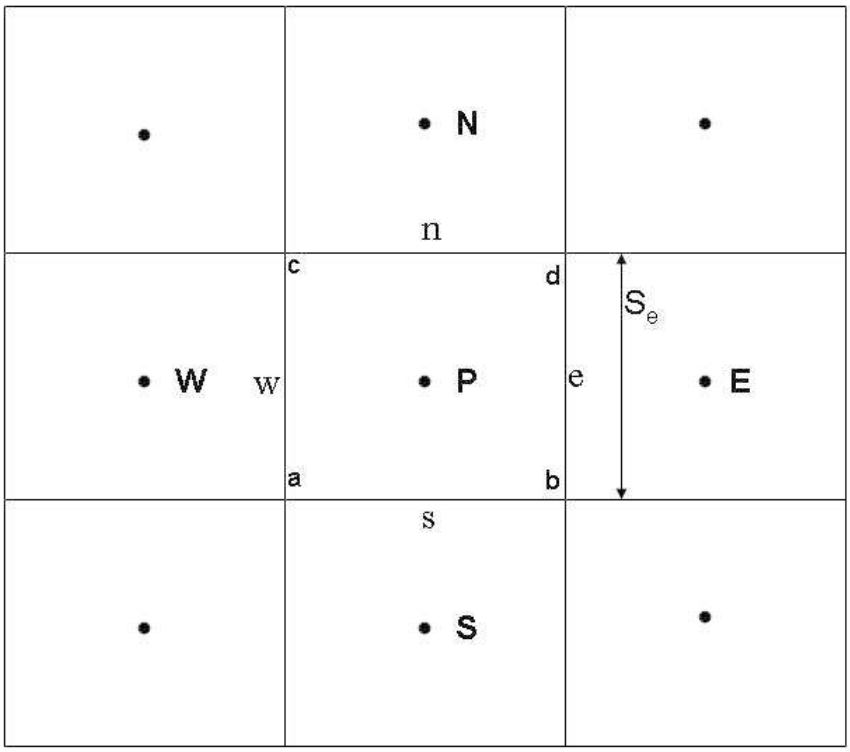

Figure 3.1: A collocated FV grid. Mean fields are stored at the center of cells. E, W, S and N denotes the centers of Eastern, Western, Southern and Northern cells, respectively. Cell faces are denoted by e, w, s and n for Eastern, Western, Southern and Northern cell faces, respectively. The area of the eastern cell face is denoted as S_e.

The velocities u^* and v^* are corrected to enforce the mass conservation through pressure correction as

$$u_e^m = \tilde{u}_e^m - \frac{S_e}{A_P^u}(p_E - p_P)^m, \tag{3.18}$$

and

$$v_n^m = \tilde{v}_n^m - \frac{S_n}{A_P^v}(p_N - p_P)^m, \tag{3.19}$$

where $p^m = p^{m-1} + p^{'}$ is the new pressure. The relation between the velocity and pressure corrections is obtained by subtracting Eq. 3.15 from Eq. 3.18:

$$u_e^{'} = \tilde{u}_e^{'} - \frac{S_e}{A_P^u}(p_E^{'} - p_P^{'}), \tag{3.20}$$

where

$$\tilde{u}_e^{'} = \tilde{u}_e^m - \tilde{u}_e^* = \frac{\sum_l A_l^u u^{'} l}{A_P}. \tag{3.21}$$

Analogously,

$$v_n^{'} = \tilde{v}_n^{'} - \frac{S_n}{A_P^v}(p_N^{'} - p_P^{'}). \tag{3.22}$$

The velocities u^m and v^m are substituted into the expressions for mass fluxes to enforce to the continuity equation, i.e.,

$$(\rho S u^{'})_e - (\rho S u^{'})_w + (\rho S u^{'})_n - (\rho S u^{'})_s + \Delta\dot{m}_P^* = 0. \tag{3.23}$$

Finally, the above expressions for $u^{'}$ and $v^{'}$ are substituted into the continuity equation leading to the pressure correction equation in the form

$$A_P^p p_P^{'} + \sum_l A_l^p p_l^{'} = -\Delta\dot{m}_P^* - \Delta\dot{m}_P^{'}, \tag{3.24}$$

where the coefficients are

$$\begin{aligned} A_E^p &= -\left(\frac{\rho S^2}{A_P^u}\right)_e, & A_W^p &= -\left(\frac{\rho S^2}{A_P^u}\right)_w, \\ A_S^p &= -\left(\frac{\rho S^2}{A_P^v}\right)_n, & A_S^p &= -\left(\frac{\rho S^2}{A_P^v}\right)_s, \\ A_P^p &= -\sum_l A_l^p, & l &= E, W, N, S. \end{aligned} \tag{3.25}$$

The term $\Delta\dot{m}_P^{'}$ is analogous to $\Delta\dot{m}_P^*$, with $\tilde{u}^{'}$ and $\tilde{v}^{'}$ replacing $\tilde{u}^*$ and $\tilde{v}^*$. Since the velocity corrections are not known prior to the solution of the pressure-correction equation, this

term is neglected in the SIMPLE algorithm [20]. Other alternatives are the SIMPLER and the PISO [20]. After the pressure-correction equation is solved, the velocities and pressure are corrected. The corrected velocities satisfy the continuity equation to the accuracy with which the pressure-correction equation is solved. However, they do not satisfy the non-linear momentum equation, so another outer iteration is needed. When both the continuity and momentum equations are satisfied to the desired accuracy, convergence is achieved.

3.2 Particle Method

The particle method is described in the context of the hybrid method and is essentially based on that of Muradoglu et al.[18]. In this approach, the fluid particles are represented by an ensemble of notional particles distributed in the physical space. Each particle has the intrinsic properties of mass m^*, position $\mathbf{X}^*$, fluctuating velocity $\mathbf{u}^*$, turbulence frequency ω^* and compositions $\boldsymbol{\phi}^*$. The particle properties are denoted by superscript * throughout the thesis unless specified otherwise. A non-uniform Cartesian grid is cast on the computational domain in order to estimate the particle fields needed in the particle evolution equations and the equations solved by the FV algorithm. The grid is also used to interpolate the particle and FV mean fields onto the particles. Note that the same grid is used in this study both for the particle and FV algorithms. The particle fields such as $\langle\rho\rangle^*$ and $(\widetilde{u_i u_j})^*$ are extracted from the particle properties using a cloud-in-cell (CIC) method[8]. The mean quantities needed in the particle evolution equations are interpolated from the nodal values of the corresponding FV or particle fields using bilinear splines. The spatial derivatives of the mean quantities that appear in the particle evolution equations are first evaluated at the nodes using second order central differences and then interpolated onto the particle locations.

The particle positions evolve according to

$$\frac{dX_i^*(t)}{dt} = \tilde{U}_i^*(t) + u_i^*(t), \tag{3.26}$$

where $\tilde{U}_i^*(t)$ is the mean velocity interpolated from the FV field onto the particle location. The fluctuating velocity evolves by

$$du_i^*(t) = \frac{1}{\langle\rho\rangle}\frac{\partial \langle\rho\widetilde{u_i u_j}\rangle}{\partial x_j}^* dt - u_j^*\frac{\partial \tilde{U}_i}{\partial x_j}^* dt - G_{ij}^*\Omega^* u_j^*(t)dt + (C_0 k\Omega)^{1/2} dW_i. \tag{3.27}$$

and the turbulence frequency and compositions by

$$d\omega^*(t) = -C_3(\omega^* - \tilde{\omega})\Omega dt - S_\omega \Omega \omega^*(t)dt + (2C_3C_4\tilde{\omega}\Omega\omega^*(t))^{1/2}dW, \tag{3.28}$$

and

$$d\boldsymbol{\phi}^*(t) = -\frac{1}{2}C_\phi\Omega(\boldsymbol{\phi}^*(t) - \tilde{\boldsymbol{\phi}})dt, \tag{3.29}$$

respectively. The particle equations (3.26,3.27,3.28) and (3.29) are integrated forward in time using the explicit second order scheme as described by Muradoglu et al.[16].

3.3 Coupled FV/Particle Algorithm

The FV and particle methods are periodically used to solve their respective equations. Each period is called an "outer" iteration that consists of FV and particle "inner" iterations. The FV and particle algorithms are coupled in a semi loosely coupled fashion[11], i.e., the FV code is run until it reaches a pseudo steady state while the particle code is run for a single time step to complete an outer iteration. The mean density and the Favre averaged Reynolds stresses are supplied to the FV code by the particle algorithm which, in turn, gets the mean velocity and pressure fields from the FV solver. Although it can be easily adopted to perform time accurate computations, the present implementation is designed to treat only the statistically stationary flows. Therefore time-averaging is performed to reduce statistical error both in the particle and FV fields. Following Muradoglu et al.[16], for a mean field Q, the time-averaged mean Q_{TA} is evaluated as follows

$$Q_{TA}^k = \left(1 - \frac{1}{N_{TA}}\right) Q_{TA}^{k-1} + \frac{1}{N_{TA}} Q_{TA}^k, \tag{3.30}$$

where the superscript k denotes the k^{th} particle time step and N_{TA} is the time-averaging factor to be specified. The time-averaging factors for the FV fields used in the FV algorithm, for the particle fields used in the FV algorithm and for the particle fields used in the particle algorithm are denoted by N_{TA}^{FV}, N_{TA}^{P2FV}, N_{TA}^{P2P}, respectively. Throughout this thesis, unless specified otherwise, the time-averaging factors are fixed at 5, 10 for N_{TA}^{FV}, N_{TA}^{P2FV} and 20 for N_{TA}^{P2P} in the initial phase of calculations and is increased to 500 when a statistically steady state is approached.

As mentioned before, although the present hybrid method is completely consistent at the level of governing equations, a full consistency at the numerical solution level may not be

achieved due to accumulation of numerical error. Therefore correction algorithms are needed to enforce the full consistency at the numerical level. Since the density field is supplied to the FV algorithm by the particle code, there are only two independent consistency conditions in the present hybrid method given by

$$\tilde{\mathbf{u}}^* = 0, \tag{3.31}$$

and

$$\langle \rho \rangle_P = q, \tag{3.32}$$

where q is the particle mass density [18]. The velocity and position correction algorithms are used to enforce the consistency conditions given by Eqs. 3.31 and 3.32, respectively. The correction algorithms are the same as those described by Muradoglu et al. [18].

3.4 Validation of the Numerical Method

The numerical properties of the present hybrid method are examined using the non-reacting and reacting bluff-body flows, which were studied experimentally by Dally et al. [6] and computationally, using the previous versions of the consistent hybrid algorithm, by Jenny et al. [10], Muradoglu et al. [15] and Liu et al. [13]. The bluff-body flows are selected as test cases since the previous versions of the hybrid algorithm failed to achieve grid convergence especially for the non-reacting case[10]. In addition, the bluff-body flames have been selected among target flames in the turbulent non-premixed flames (TNF) workshop [29] due to their relevance to numerous engineering applications such as bluff-body stabilized combustors widely used in industrial applications because of their enhanced mixing characteristics, improved flame stability and ease of combustion control [6]. Besides their practical significance, the bluff-body flows studied here provide an excellent but challenging test case for the numerical solution algorithms as well as the chemistry and turbulence models due to their simple and well defined initial and boundary conditions, and their ability to maintain the flame stabilization for a wide range of inlet flow conditions with a complex recirculation zone [6, 15].

3.4.1 Boundary Conditions

The geometry and the computational setup of the bluff-body flows are sketched in Fig.(3.2). The inlet and boundary conditions are the same as those used by Jenny et al. [10] for the non-reacting case and as those used by Muradoglu et al. [15] for the reacting case. A fully developed turbulent pipe flow is assumed in the jet region and variances of velocity are interpolated from the experimental data. Mean turbulent shear stresses are calculated as

$$\widetilde{u_x u_y} = \rho_{12}(u_x^2 u_y^2)^{0.5}, \tag{3.33}$$

where u_x and u_y are axial and radial components of the fluctuating velocity, $\rho_{12} = -0.4$ and $\rho_{12} = 0.5(y/R_j)$ in the coflow and jet regions, respectively. Particle fluctuating velocity components are specified so that they have zero mean at the inlet. Turbulent frequency at the inlet is specified using

$$\tilde{\omega} = \frac{P}{k} = -\frac{\widetilde{u_x u_y}}{k}\frac{\partial \widetilde{U}}{\partial y}, \tag{3.34}$$

where k is the turbulent kinetic energy and P is the mean turbulent energy production rate. A perfect slip is assumed on the bluff-body. The outlet pressure is fixed to atmospheric pressure ($p_0 = 1$ atm). The inlet boundary conditions are also used as initial conditions.

As sketched in Fig.(3.2), a rectangular computational domain with 0.75m ($15D_b$) in the axial direction and 0.15m ($3D_b$) in the radial direction is selected, where D_b stands for the diameter of the bluff-body. Inlet boundary conditions are specified at $x = 0$. The radius of the fuel jet is $R_j = 0.0018$ m and the radius of the bluff-body is $R_b = 0.025$ m. The outer boundary in the radial direction is located at $y = 0.15$ m.

The mean velocity is specified in the jet region assuming a fully developed turbulent pipe flow in the same way as Jenny et al. [10]. The bluff-body is treated as a perfect-slip wall. In the coflow region the experimental data, which is available from the Internet [14], is interpolated to corresponding locations. At first region where jet flows in, density has been set to fuel density and in the other two regions density has been set to air density. Properties are interpolated onto particles at the inlet.

Outlet boundary properties are set at $x = 0.75$ m. At the outlet, pressure is set to atmospheric pressure 1 atm. Particles leaving the computational domain at outlet are eliminated.

At the centerline, symmetry boundary conditions are applied both for FV solver and particle method. Particles crossing the centerline are reflected back into the computational domain.

The computational grid is stretched in the jet region and also in the jet/bluff-body and bluff-body/coflow shear layers as the flow properties are expected to change most rapidly in these regions. The computational grid is also stretched in the recirculation region. Some properties of the computational grids used here are summarized in Table (3.1).

A non-reacting bluff-body flow labeled as B4C1 and reacting bluff-body flow labeled as HM1E are selected for validation purpose. The jet velocity is 61 m/s, and coflow velocity is 20 m/s in the B4C1 and the jet velocity is 108 m/s, and coflow velocity is 35 m/s in the HM1E. The number of particles per cell is fixed at 50, which has been shown previously to be sufficient to reduce the associated numerical error below 5% [16]. Maximum outer iterations are set to 15 for the FV solver.

As mentioned before, the present hybrid algorithm is designed to simulate the statistically stationary flows. Therefore the statistical stationarity is first examined both for the B4C1 and HM1E flows. For these purpose, the mean axial velocity and mean turbulent kinetic energy are monitored at six selected locations (see, e.g., Table (3.2)) and are plotted as a function of particle time steps in Figs. 3.2 and 3.4 for the non-reacting and reacting cases, respectively. As can be seen in these figures, the statistically stationary state is reached rapidly in the case of non-reacting flow while it takes about 8000 particle time steps for the reacting case. The smoothing effects of time averaging can be clearly seen in these figures, i.e., after about 5000 particle time steps in both cases.

The grid convergence of the method is also examined. For this purpose, the grid is successively refined and the spatial error is quantified as function of the number of grid cells denoted by M^2. The profiles of mean axial velocity and the rms fluctuating velocity computed using 64×64, 80×80, 96×96 and 128×128 are plotted in Figs. 3.5 and 3.6 at locations $x/D_b = 0.6$ and $x/D_b = 1$ for the non-reacting and reacting cases, respectively. The grid convergence is also quantified in Figs. 3.7-3.8. In these figures, the mean axial velocity and rms axial velocity have been plotted at selected locations as summarized in Table 3.2. The spatial error is defined as

$$\epsilon = \frac{|Q_M - Q_\infty|}{\max(|Q_\infty|, \kappa|Q_{ref}|)} \tag{3.35}$$

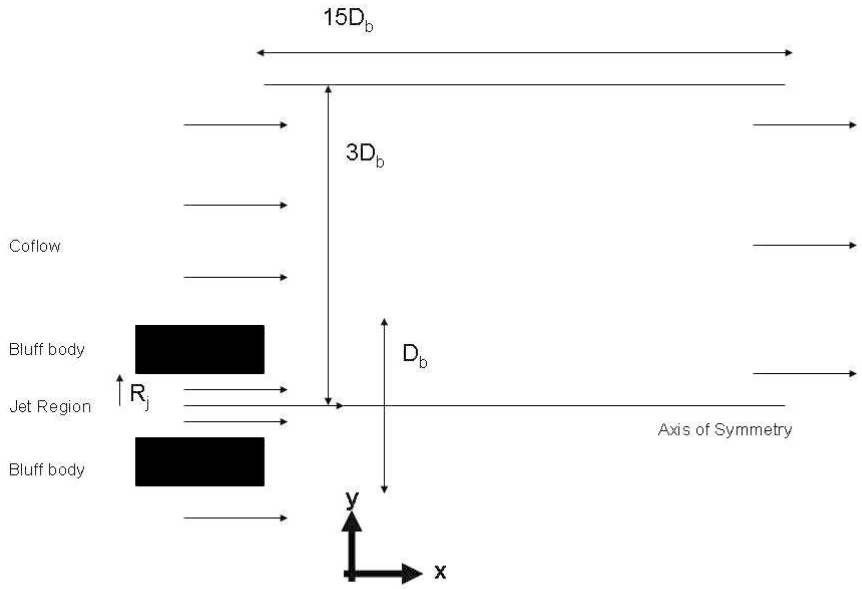

Figure 3.2: Sketch of the bluff-body flows. Radius of the jet region and the diameter of the bluff-body are denoted by R_j D_b, respectively. Axial and radial lengths of the computational domain are set to $15D_b$ and $3D_b$, respectively.

where Q_M is the numerical result obtained on a grid containing M^2 grid cells, Q_∞ is the grid independent value obtained using the Richardson's extrapolation as $M \to \infty$, Q_{ref} is the reference value taken as the largest of Q at the inlet and κ is taken to be 0.2. This cut off procedure is used to avoid singularities at locations where the mean quantities approach zero. The spatial error is plotted in Figs. 3.7 and 3.8. These figures clearly show the second order spatial accuracy of the present hybrid method. It is deduced from Figs. 3.7 and 3.8 that a 96×96 grid is sufficient to reduce the spatial error below 5% for all the six locations.

After showing the statistical stationarity and grid convergence of the hybrid method, it is first applied to the non-reacting case using a 96×96 grid. The mean fields are compared with the experimental data in Figs. 3.9-3.12. As can be seen in these figure, there is generally a reasonably good agreement between the computational and experimental results for all mean fields. In addition, although not shown here, the present results agree very well with

the results obtained with the old version of the hybrid algorithm. Alto ugh not included in this thesis, the new hybrid algorithm is also successfully applied to compute the non-reacting bluff-body flow using even finer grids, i.e., grids containing 192×192 and 256×256 grid cells. It is emphasized here that no vortex shedding is observed even on 256×256 grid showing the robustness of the present method.

After showing the grid convergence and accuracy of the present hybrid algorithm for the non-reacting bluff-body flow, it is applied to the reacting bluff-body flow. A 96×96 grid is used and 50 particles per cell is employed. Time-averaging factors are again set to 5, 20, 500 for N_{TA}^{FV}, N_{TA}^{P2FV} and N_{TA}^{P2P}, respectively. Convergence histories of mean axial velocity and turbulent kinetic energy have been already shown in Fig. **??** to show statistical stationary state. As mentioned before, a statistically stationary solution is reached approximately after 10000 particle time steps. Then the mean fields are compared with the available experimental data. For this purpose, the mean axial velocity profiles are plotted in Fig. 3.13 together with the experimental data at various axial locations. As can be seen in this figure, the predicted mean axial velocity profiles are overall in a good agreement with the experimental data considering the simplest The mean radial velocity profiles are shown in Fig. 3.14. Although there is probably more measurement error in the mean radial velocity data since the rms fluctuating radial velocity is almost ten times greater than its mean value, the computational results are again in a very good agreement with the experimental data for the mean radial velocity profiles. Finally the rms fluctuating velocity profiles are plotted in figures 3.15 and 3.16 at various axial locations. As seen in these figures, the computed rms fluctuating velocity profiles are also well predicted for the reacting case.

Grid	$Region : 1$	$Region : 2$	$Region : 3$
64x64	8	40	16
80x80	10	50	20
96x96	12	60	24
128x128	16	88	32

Table 3.1: Number of cells used in three regions in different grids. Region 1, 2 and 3 denote jet, bluff-body and coflow regions, respectively.

	Axial distance	Radial distance
Location 1	$0.6D_b$	0
Location 2	$0.6D_b$	R_j
Location 3	$0.6D_b$	mid bluff-body = 13.4 mm
Location 4	$1.0D_b$	0
Location 5	$1.0D_b$	R_j
Location 6	$1.0D_b$	mid bluff-body = 13.4 mm

Table 3.2: Six selected locations in the bluff-body computational domain to monitor grid convergence. $D_b = 50$ mm is bluff-body diameter and $R_j = 1.8$ mm is jet radius.

3.5 Summary

Newly developed hybrid method is tested for the non-reacting and reacting test cases. A complete grid convergence is achieved both the non-reacting and reacting cases and a 96×96 grid is found to reduce the spatial error below 5%. The new hybrid method is shown to be very robust and is not too sensitive to relaxation parameters. Therefore it is much easier for non-experts to use the present hybrid method for modeling of the reacting turbulent flows.

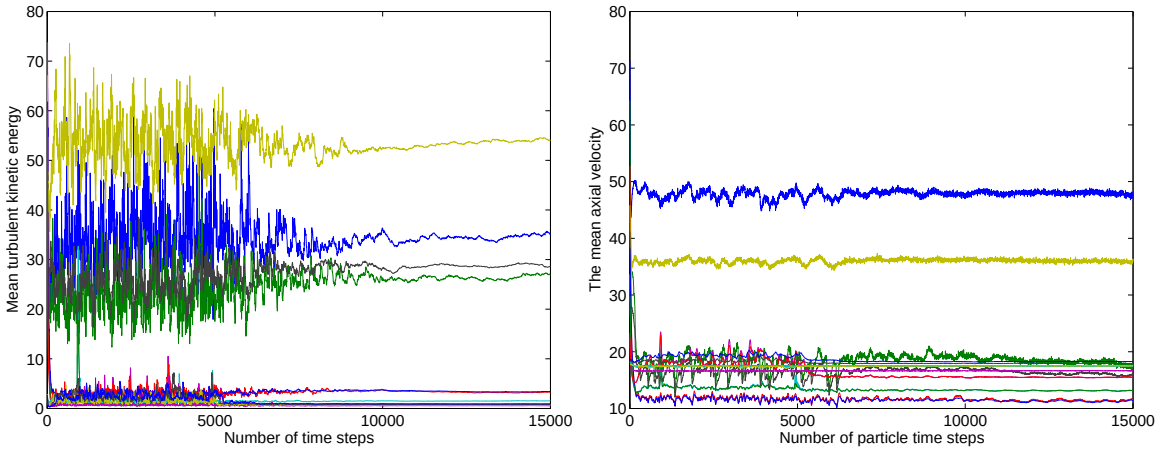

Figure 3.3: Convergence histories of the mean turbulent kinetic energy (left plot) and the mean axial velocity (right plot) for non-reacting bluff-body flow.

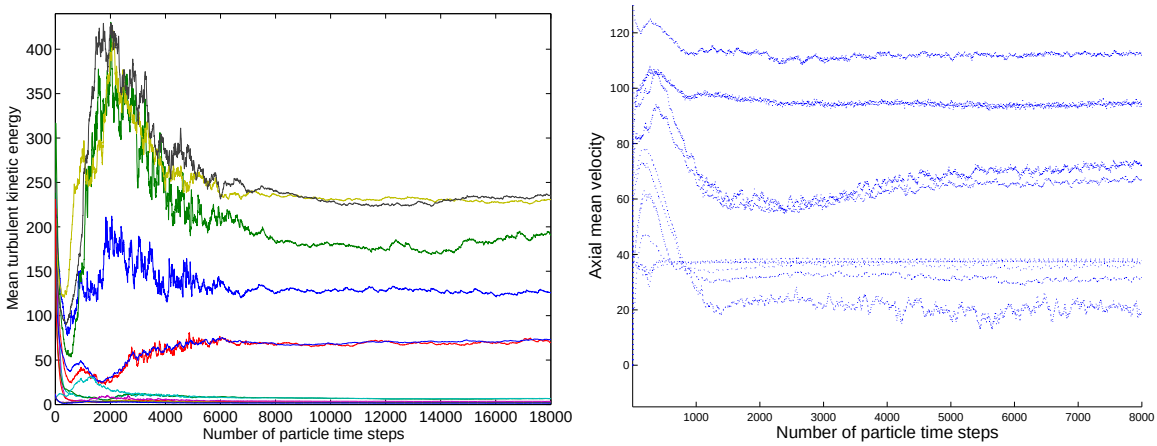

Figure 3.4: Convergence histories of the mean turbulent kinetic energy (left plot) and the mean axial velocity (right plot) for reacting bluff-body flow.

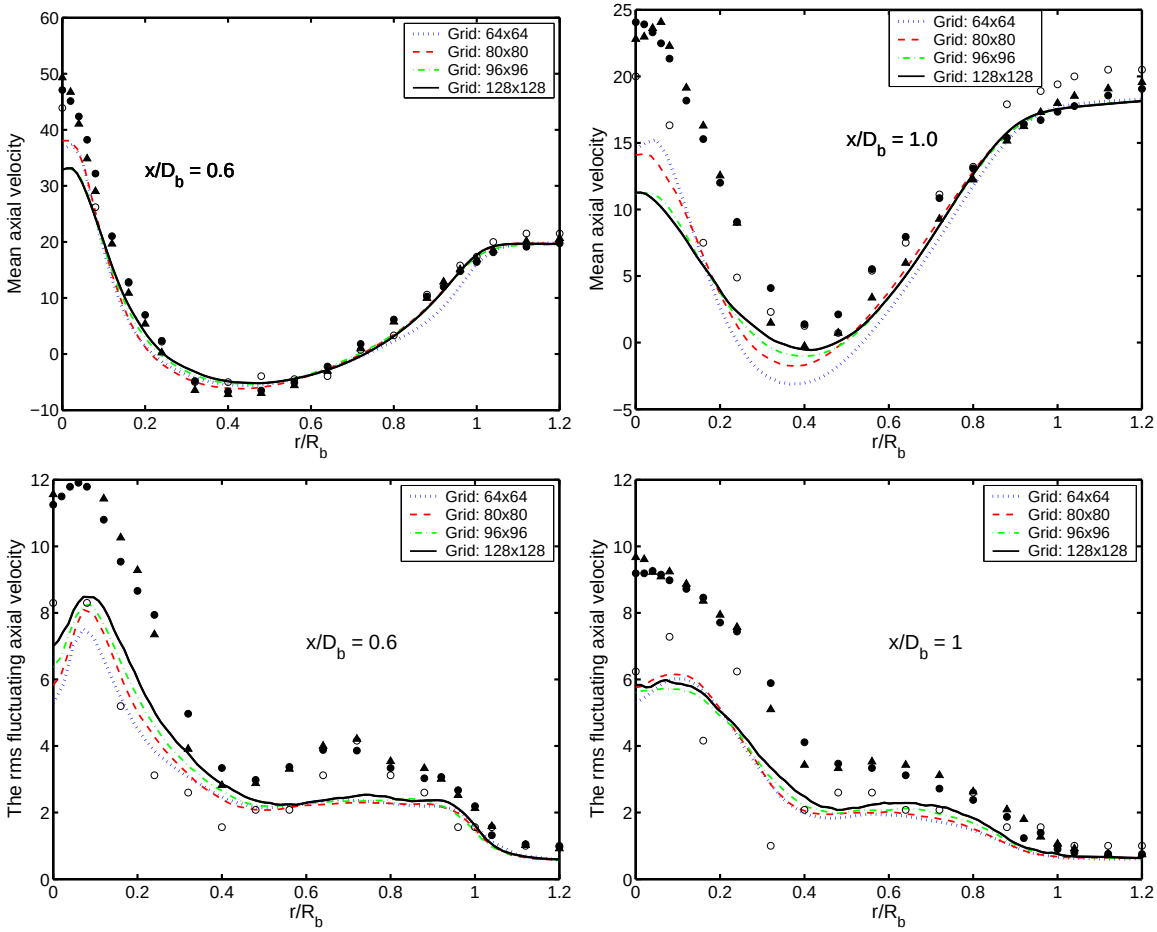

Figure 3.5: Non-reacting bluff-body flow. Profiles of mean axial velocity (top plots) and the rms axial velocity (bottom plot) at the axial locations $0.6D_b$ (left plots) and D_b (right plot) computed using 64×64, 80×80, 96×96 and 128×128 grids.

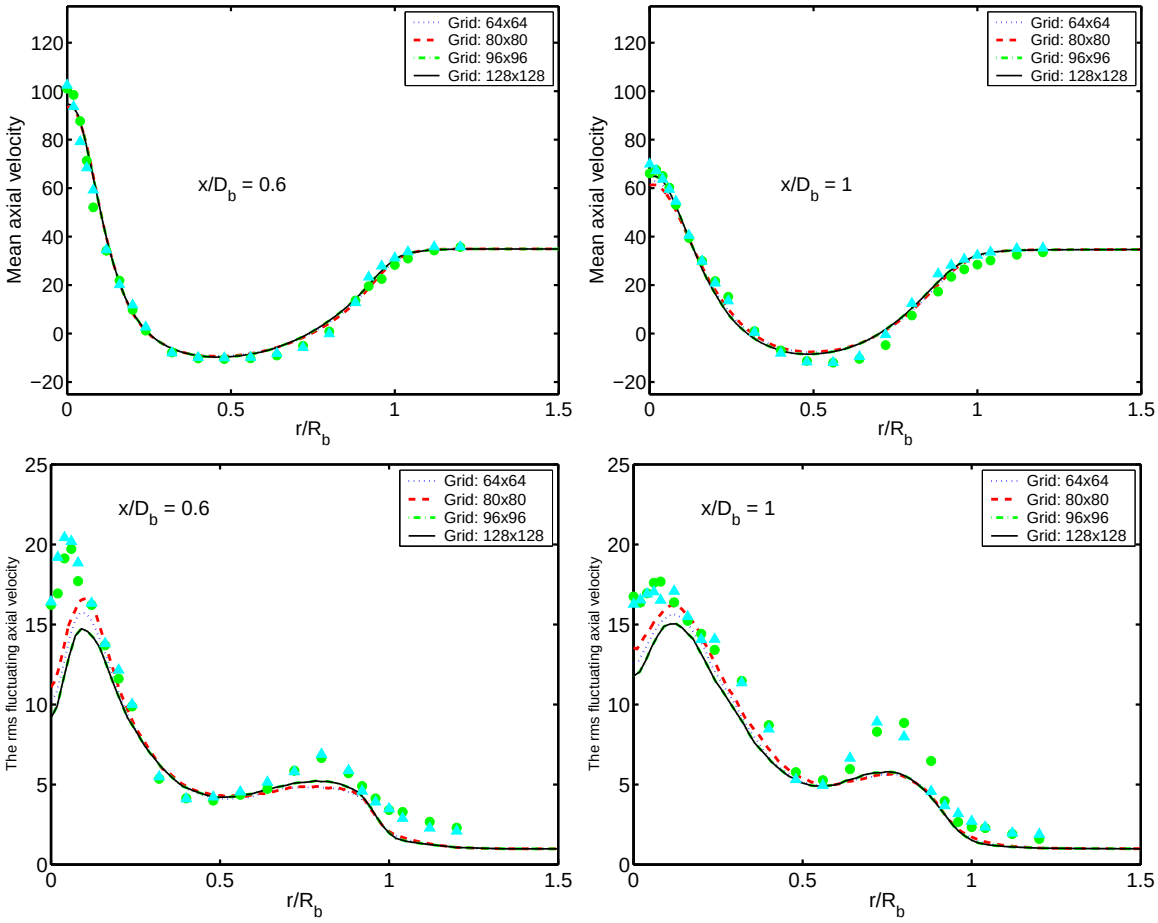

Figure 3.6: Reacting bluff-body flow. Profiles of mean axial velocity (top plots) and the rms axial velocity (bottom plot) at the axial locations $0.6D_b$ (left plots) and D_b (right plot) computed using 64×64, 80×80, 96×96 and 128×128 grids.

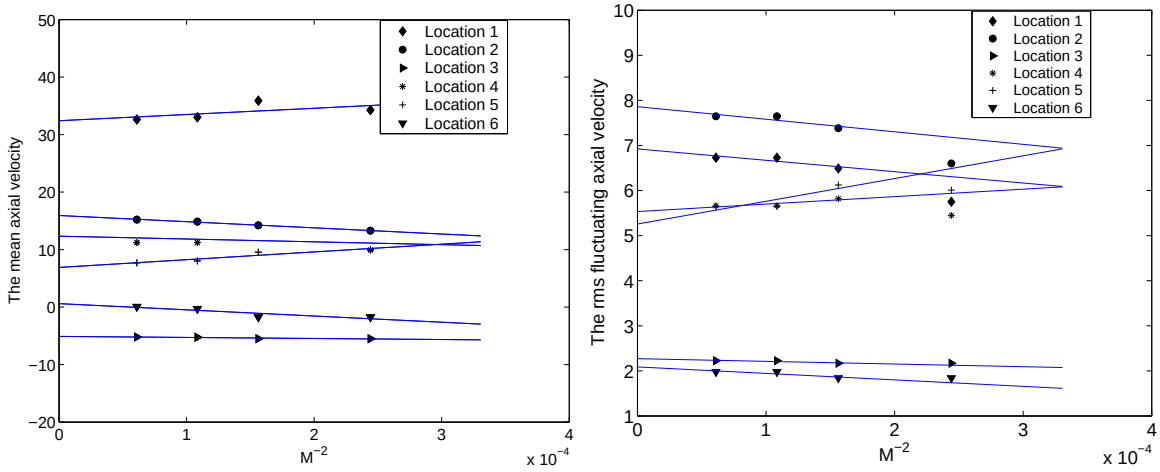

Figure 3.7: Non-reacting bluff-body flow. Time-averaged mean quantities against the inverse of grid size M^{-2} at selected locations showing the expected second order spatial accuracy. Solid lines are linear least square fits to data

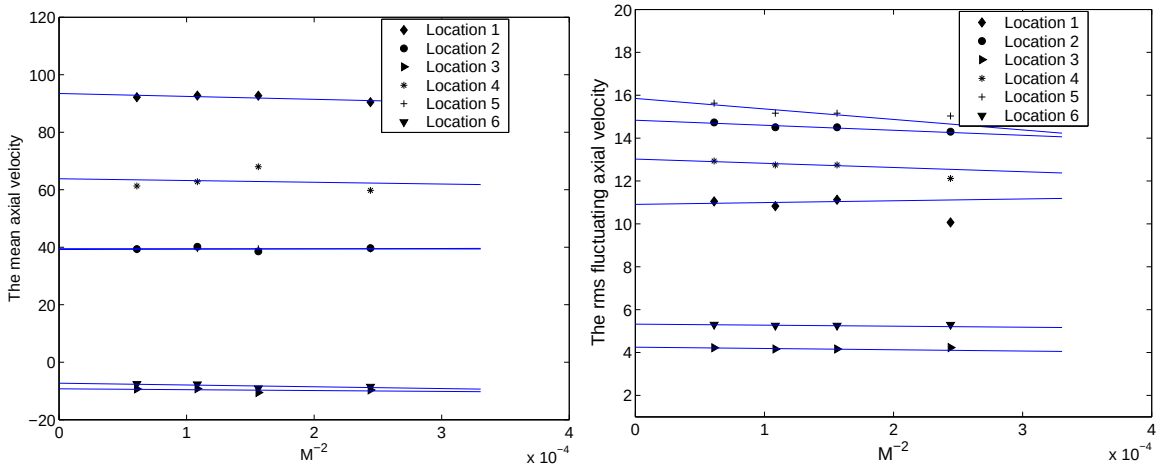

Figure 3.8: Reacting bluff-body flow. Time-averaged mean quantities against the inverse of grid size M^{-2} at selected locations showing the expected second order spatial accuracy. Solid lines are linear least square fits to data

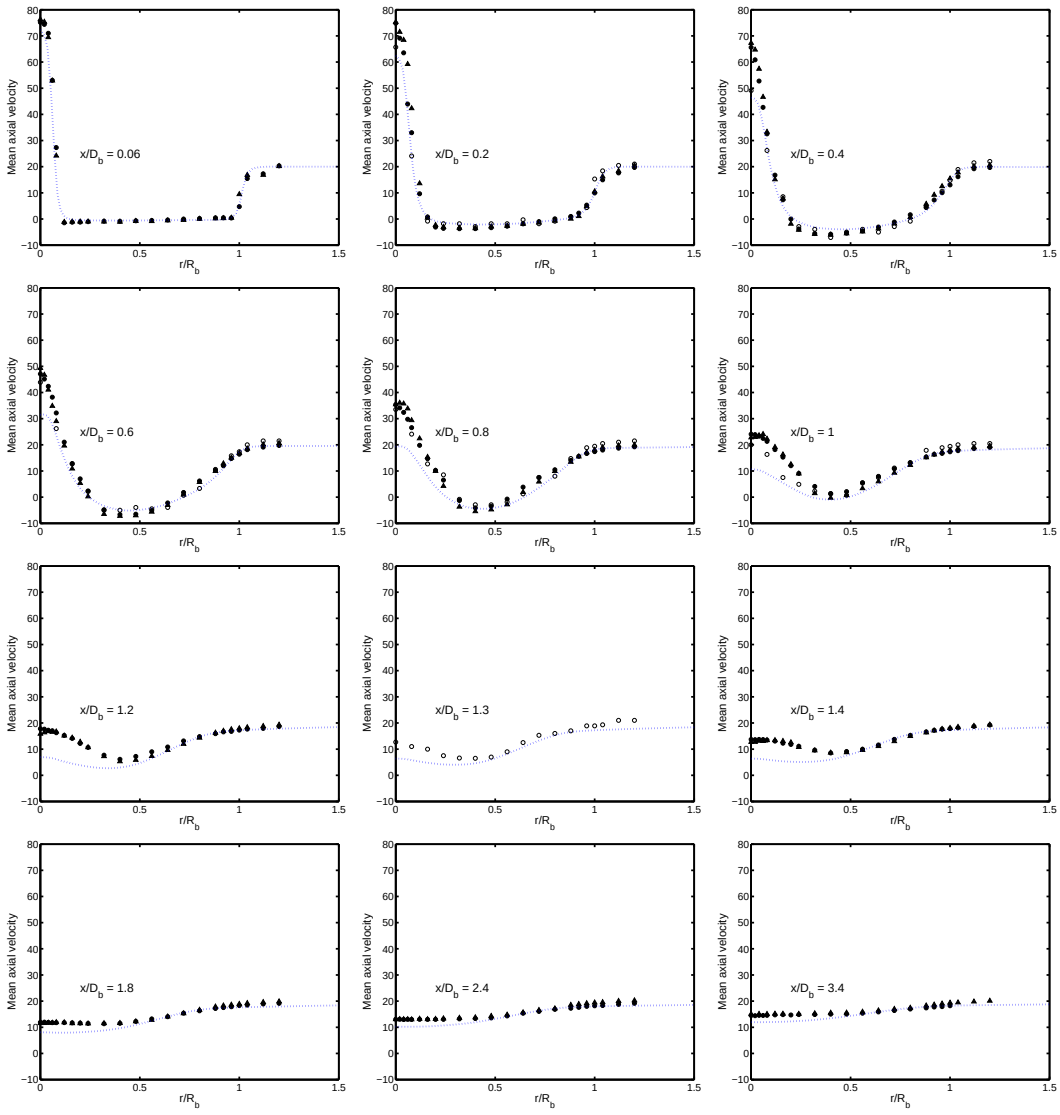

Figure 3.9: Profiles of mean axial velocity for non-reacting bluff-body flow in various axial locations.

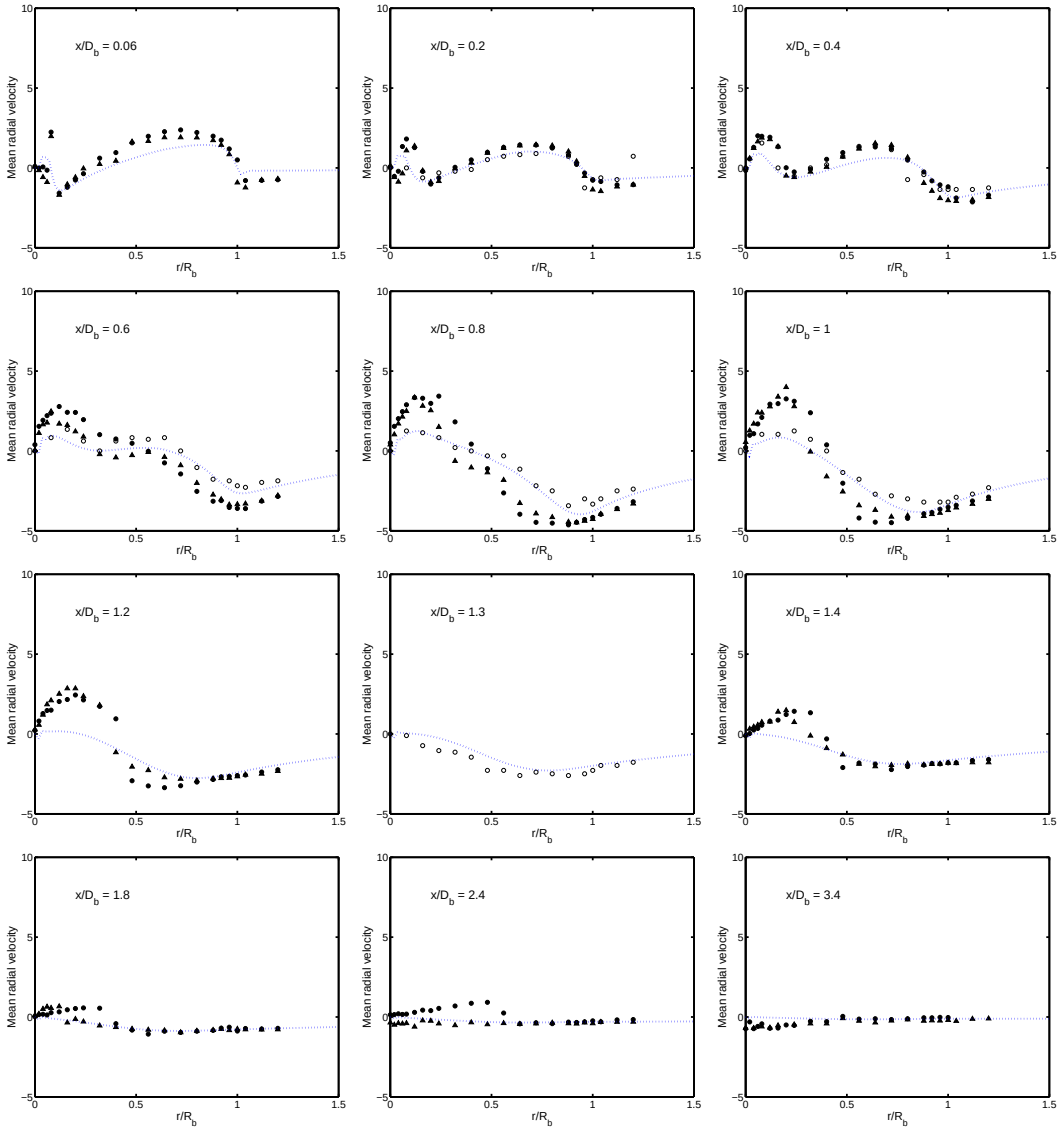

Figure 3.10: Profiles of mean radial velocity for non-reacting bluff-body flow in various axial locations.

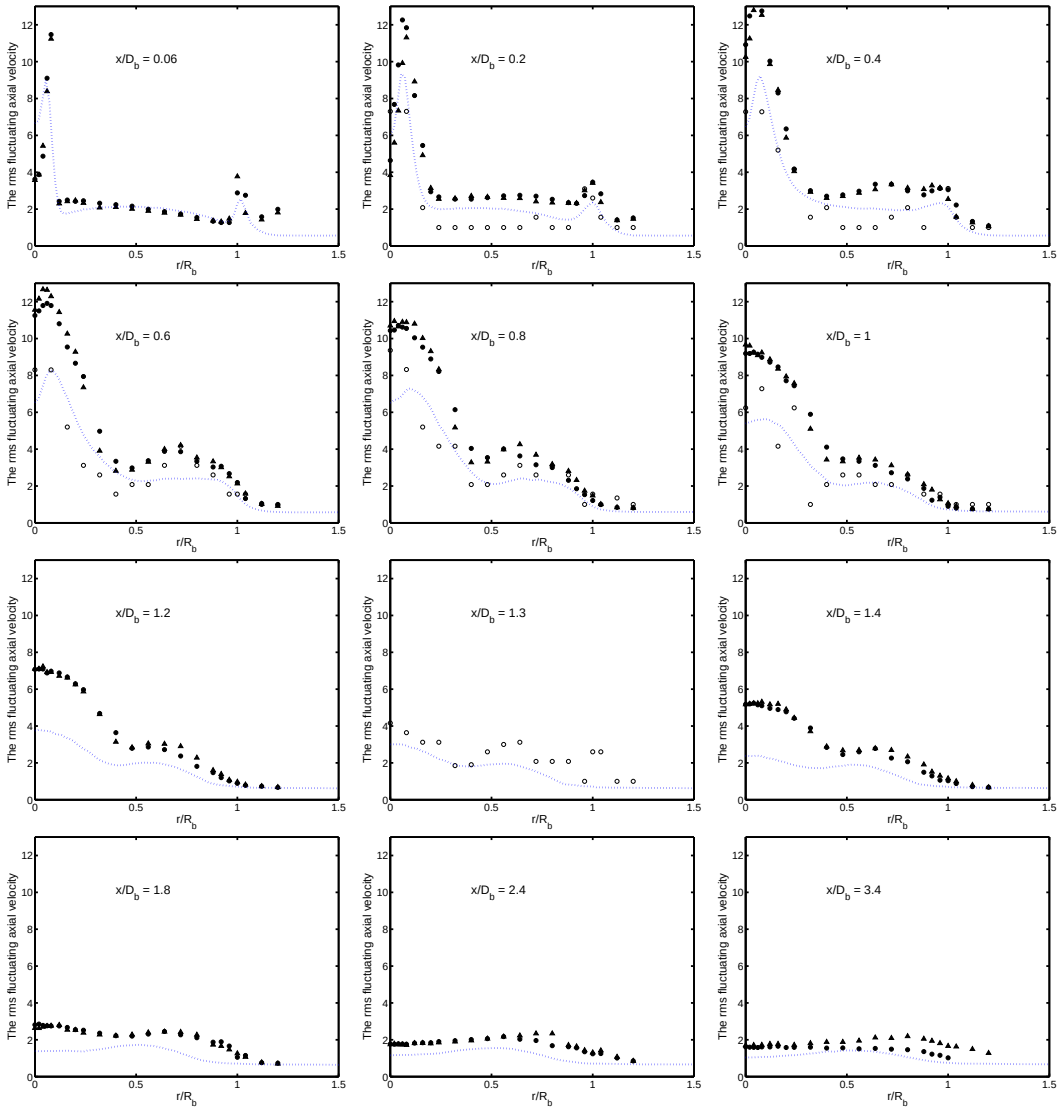

Figure 3.11: The rms fluctuating axial velocity profiles for non-reacting bluff-body flow in various axial locations.

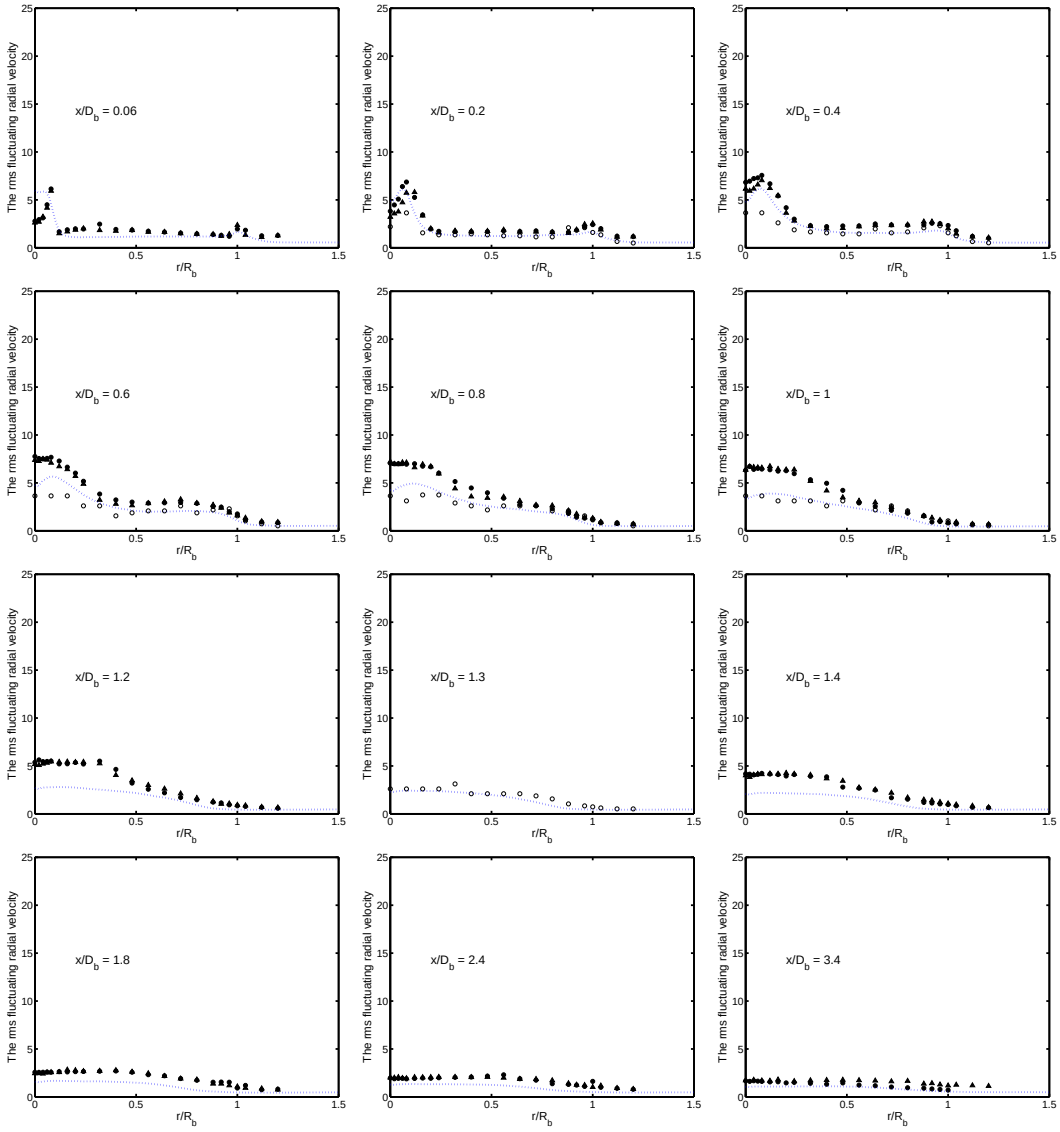

Figure 3.12: The rms fluctuating radial velocity profiles for non-reacting bluff-body flow in various axial locations.

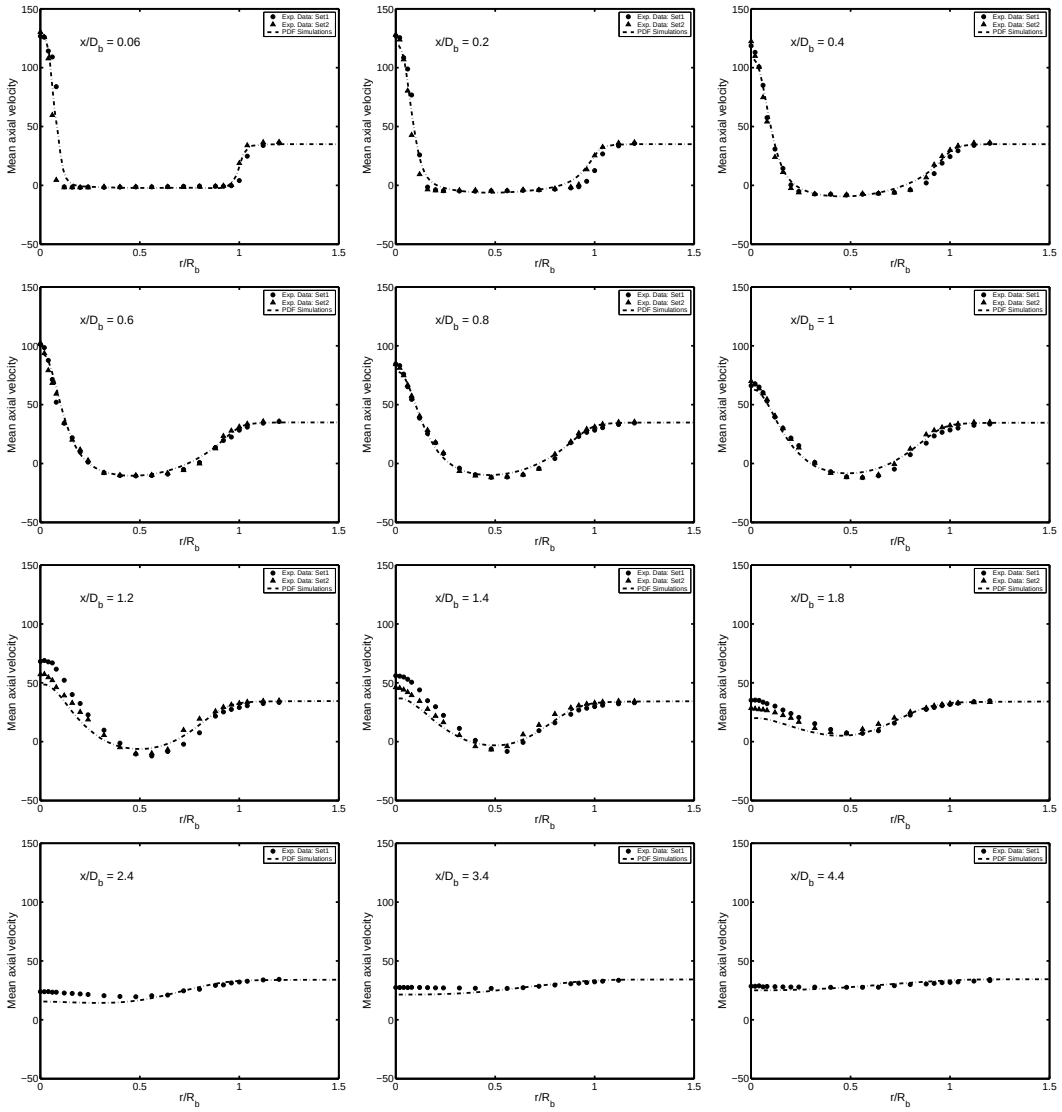

Figure 3.13: Profiles of mean axial velocity for reacting bluff-body flow in various axial locations.

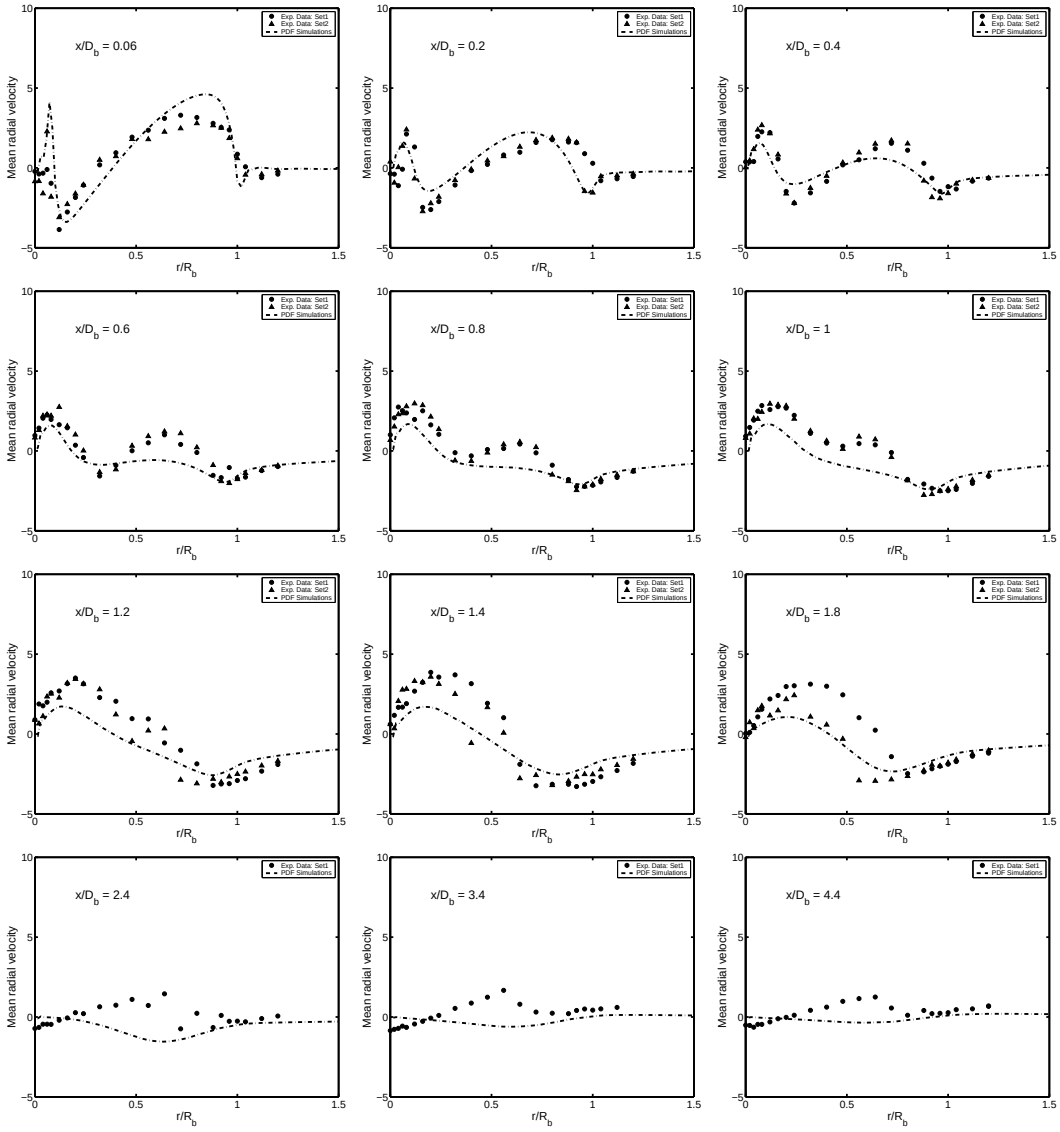

Figure 3.14: Profiles of mean radial velocity for reacting bluff-body flow in various axial locations.

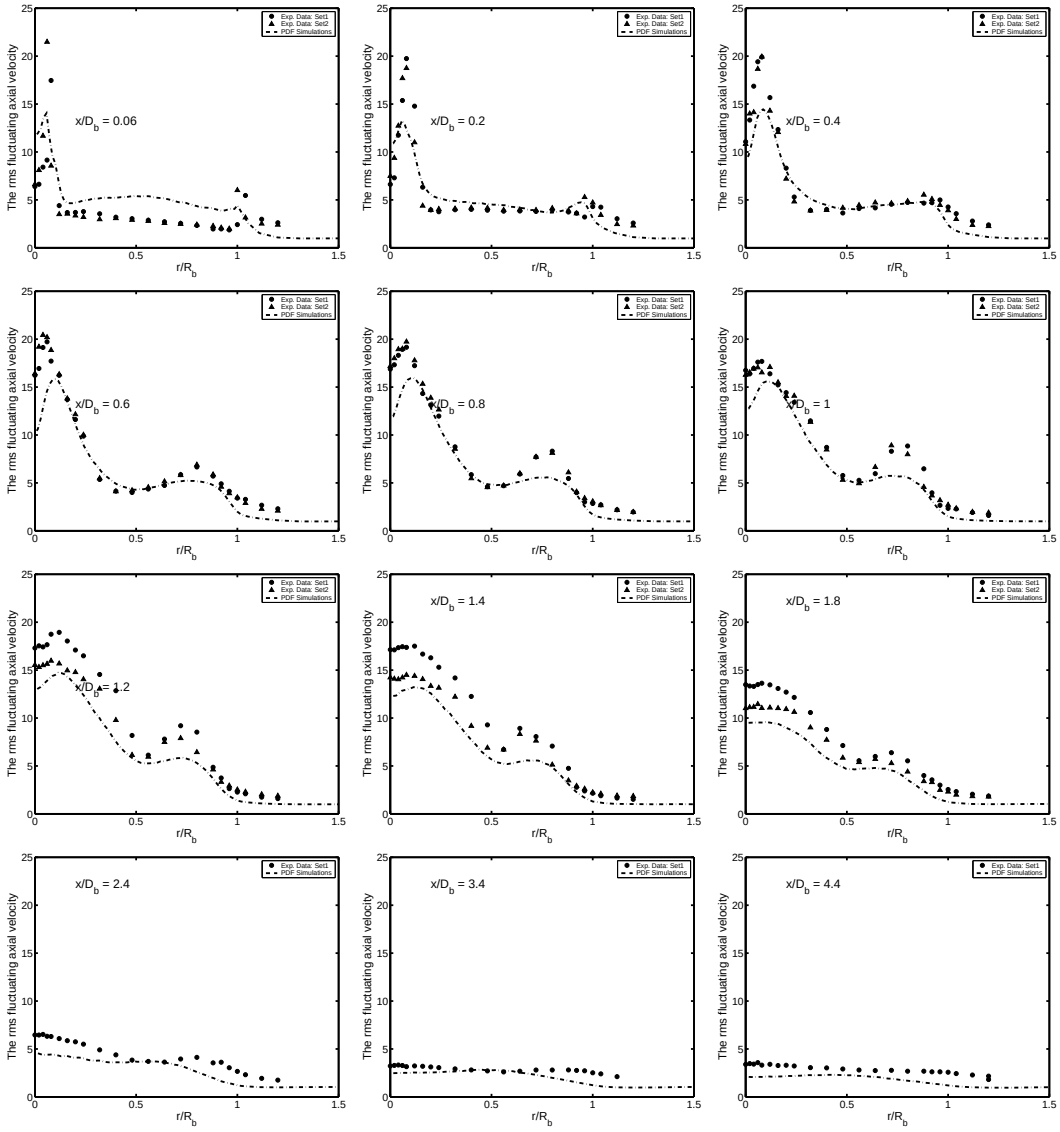

Figure 3.15: Profiles of rms fluctuating axial velocity for reacting bluff-body flow in various axial locations.

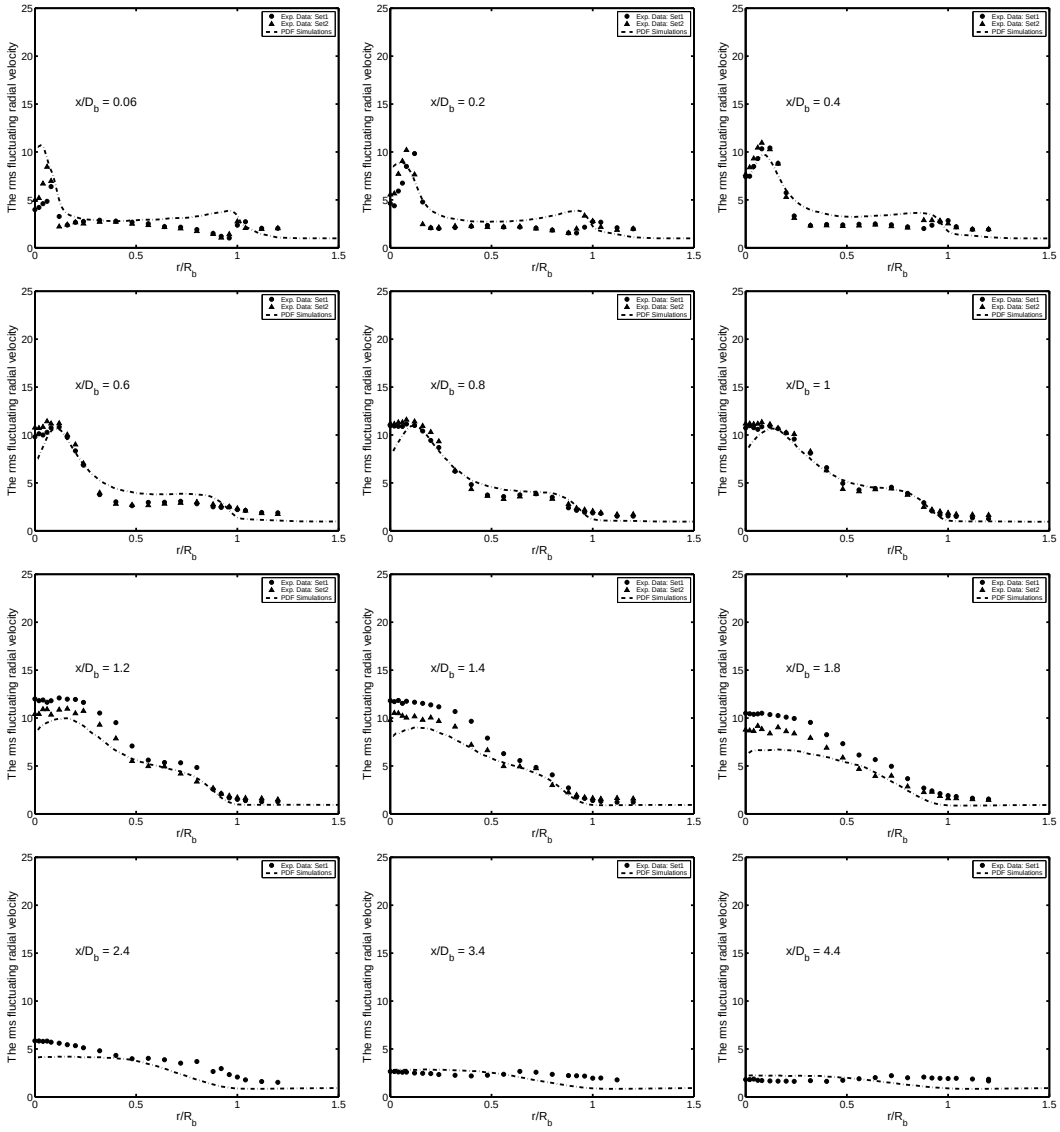

Figure 3.16: Profiles of rms fluctuating radial velocity for reacting bluff-body flow in various axial locations.

Chapter 4

PERFORMANCE OF VELOCITY MODELS

In the previous chapter, the new hybrid solver has been validated and grid convergence of the method has been demonstrated both for non-reacting and reacting bluff-body flows using SLM as the velocity model. The hybrid method is used in this chapter to study the comparative performance of simplified Langevin Madel (SLM), Lagrangian isotropization of production model (LIPM) and Lagrangian Speziale-Sarkar-Gatski model (LSSG). The non-reacting and reacting bluff-body flows are used again as test cases and computational results are compared with the available experimental data. In addition, an analysis is performed to assess the sensitivity of the computed results to the velocity model coefficients and an attempt is made to optimize the model coefficients.

The velocity models are described in details in Chapter 2. As discussed by Pope [22], the velocity models are usually constructed such that they correspond to existing Reynolds stress models at the second moment closure level. In addition, the usual guiding principles such as realizability, boundedness, the behavior in the isotropic turbulence limit are used to model the unclosed terms. However there are still some undetermined coefficients that are usually specified based on the experimental data or direct numerical simulation (DNS) results. These coefficients are not usually optimized mainly due to the lack of efficient and accurate numerical solution algorithms required to perform extensive numerical simulations. As a first step in this direction, the new hybrid algorithm is used here to perform extensive computational simulations in order to assess the comparative performance of the SLM, LIPM and LSSG velocity models and to show the sensitivity of the computational results to the model coefficients. It is of course not possible to draw solid conclusions based on the results obtained just for bluff-body flows and more extensive parametric study using more diverse test cases is required and this is left as a future study.

4.1 Sensitivity Analysis and Optimization of the Velocity Models

The experimental data are used to assess the performance of the velocity models. The measurements for the bluff-body flows were first performed by Dally et al. [6] and the same measurements were repeated twice more recently by the same group[14]. In this study, we consider the two recent experimental data and take a simple average of these two sets of data to obtain the experimental values that are assumed to be the "exact" values. It is stressed here that there are significant differences between the sets of experimental data measured by the same group in the same laboratory mainly due to complex flow field involved in the bluff-body flows and difficulty to measure mean quantities in the thin jet region. The turbulent shear stresses are not taken into account in evaluating the performance of the velocity models since measurement errors are considerably higher in the turbulent shear stress data. The experimental data are assumed to be *exact* and the normalized error is defined as

$$\epsilon = \frac{|Q_N - Q_{exp}|}{\max(|Q_{exp}|,\kappa|Q_{ref}|)} \tag{4.1}$$

where Q_N is the numerical result, Q_{exp} is the experimental result, Q_{ref} is the reference value taken as the largest of Q_N at the inlet and κ is taken to be 0.2. This cut off procedure is adopted to avoid singularities at locations where some mean quantities approach zero. Throughout this study the normalized errors are calculated only for mean axial velocity and the fluctuating rms velocities.

4.1.1 Sensitivity Analysis of LIPM

Following Pope [22] we consider olny the coefficient α_2 for the parametric study of the LIPM model. The normalized percentage errors for axial velocity, the rms fluctuating velocities in the jet region and overall error are plotted in Fig. 4.1 for various values of α_2. As can be seen in this figure, the smaller values of α_2 generally improves the predictions in the jet region for non-reacting bluff-body flow. However the same improvement is not observed in reacting case where the results seem to be essentially insensitive to changes in α_2. Another important observation is that the normalized error is more sensitive to the changes of α_2 in jet region for non-reacting case but not for the reacting case. It can be seen from Fig. 4.1 that the best error reduction is achieved for $\alpha_2 = 2.1$. Hence we propose this values as

a new coefficient for LIPM and call this model as the modified LIPM denoted by M-LIPM model throughout this work. For coefficients less than 2.0, the length of the recirculation zone is increasing in both reacting and non-reacting cases compared to experimental data and over predicting the mean axial velocity in the jet region. Hence further decrease in this coefficient does not lead to any improvement yet the flow structure changes considerably. It has also been found that, when α_2 is chosen between 2.0 and 3.9, length of recirculation zone does not change considerably. This is a very important result since the accurate prediction of the length of recirculation zone is crucial as most of the turbulent, chemical and mixing processes occur in the recirculation region.

4.1.2 Sensitivity Analysis of LSSG Model

In the LSSG model, the model coefficients C_2, C_5 and α_2 are free for modifications. While α_2 is directly related to the model coefficients α_1 and α_3 such that increasing α_2 leads to an increase in α_3 and a decrease in α_1, the model coefficient α_2 is independent of α_3 and α_1. It has been found that α_3 does not have an important influence on computational results in the range considered in this study. γ_5 and γ_6 are investigated through C_5 by varying C_5 in the range of 0.0 and 1.4. It has been found that modifying C_5 from 0.4 to 0.35 significantly improves prediction of mean axial velocity, the rms axial and radial velocities in non-reacting case but not for reacting case. The standard values are found to be nearly optimal for the reacting case. It has been also found that, as C_5 coefficient is decreased, the mean axial velocity increases and the length of recirculation zone changes considerably both for the reacting and non-reacting cases. However the length of the recirculation zone decreases as the coefficient C_5 is increased. It has been found that LSSG model is the most sensitive to C_5 and $C_5 = 0.35$ is nearly optimal for the bluff-body flows. Therefore the LSSG model with $C_5 = 0.35$ is called the modified LSSG model and denoted by M-LSSG throughout this work. In the Fig. 4.2 all models are compared in terms of normalized errors.

4.2 A Comparative Study of Velocity Models

The performance of the velocity models including the modified LIPM and LSSG models is assessed in this section. The comparison is done by comparing normalized errors for each flow case for the jet region and for the overall computational domain separately.

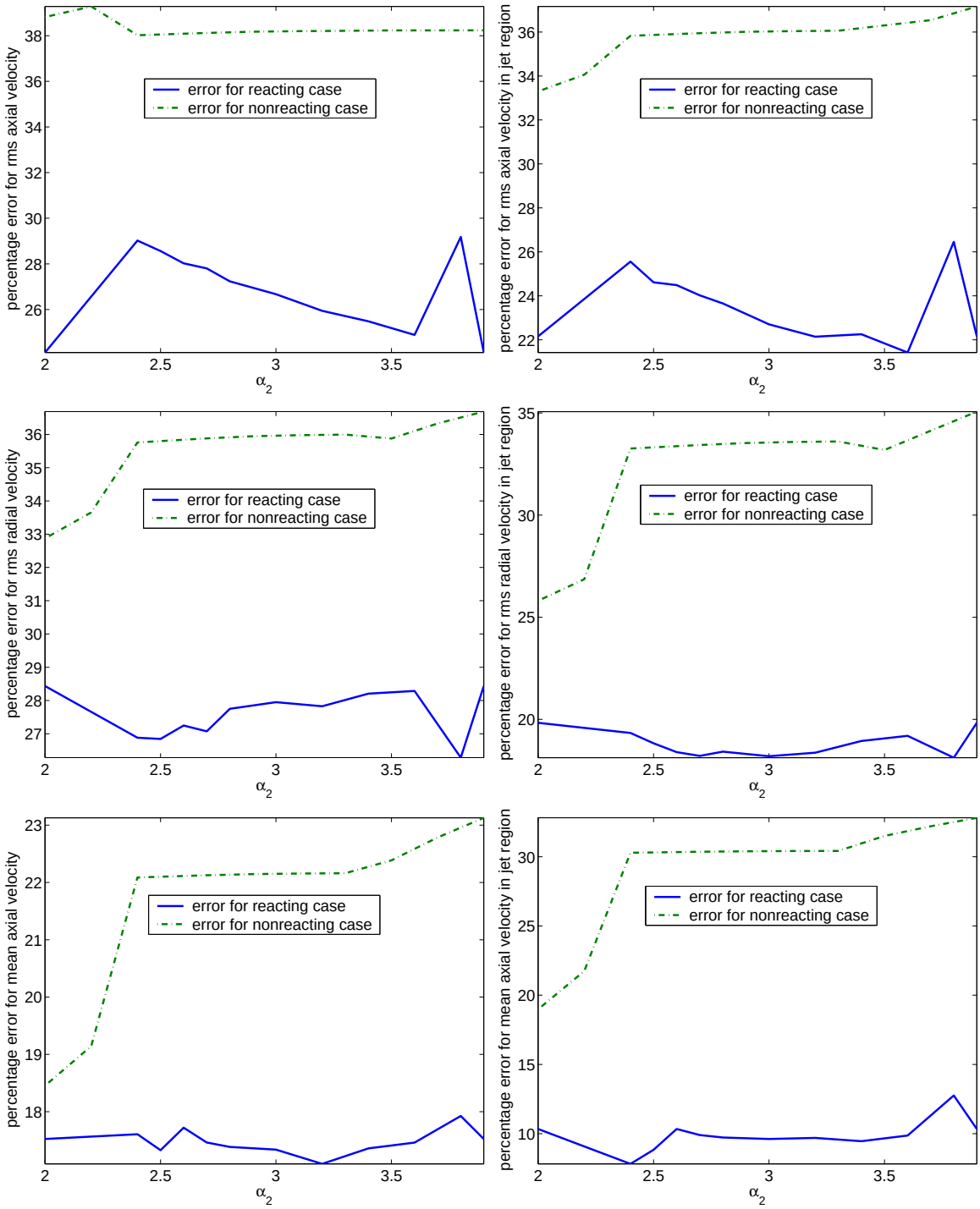

Figure 4.1: Percentage normalized error for various values of α_2 in the LIPM model. Dashed dotted lines denote errors for non-reacting case and solid lines denote errors for the reacting case.

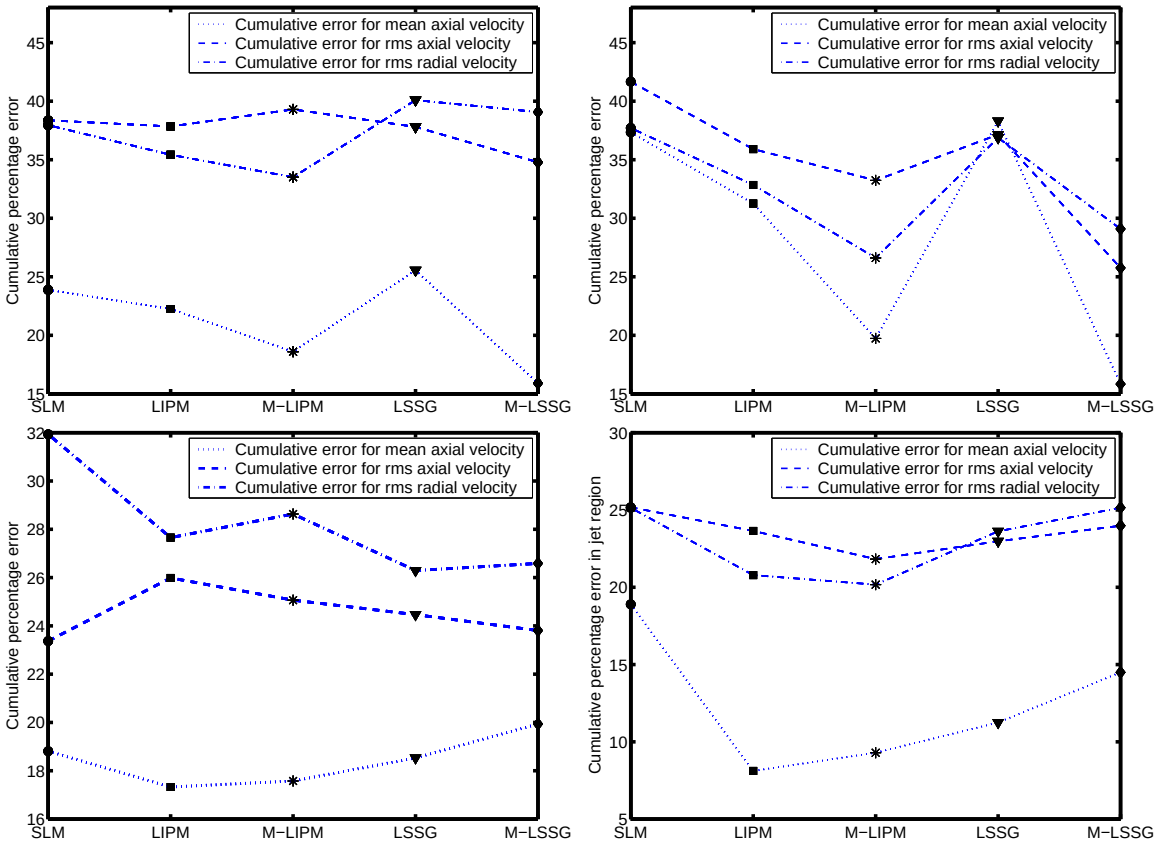

Figure 4.2: Percentage normalized error based on the bluff-body simulations using different velocity models. The figures in top row are percentage errors for nonreacting case and the figures in bottom row are percentage errors for reacting case.

4.2.1 Non-reacting Bluff-Body Simulations

To demonstrate the performance of velocity models, the computed mean fields are compared with the experimental data and the accuracy of predicted mean fields are quantified. Radial profiles of the mean axial velocity and the rms fluctuating velocities are presented at axial locations $x/D_b = 0.2, 0.4, 0.8, 1.2, 1.4$ and 2.4. In Sections 4.1.1 and 4.1.2 modified LIPM and LSSG are found superior to other models in terms of predicting mean fields, especially in the jet region, in which the improvement is almost 25%. In Fig. 4.3 it is clear that with modified LIPM and LSSG the axial velocity is captured very well compared to other models, especially in the jet region. In Figs. 4.5 and 4.6 the fluctuating axial and radial velocities are presented, respectively. Although, all of the models predict the mean fields reasonably well, modified LSSG and LIPM outperform especially in the jet region. It should be also noted that assessment is based on the assumption that the *exact* value is the simple average of two consecutive experiments, which obviously involves some uncertainties.

Considering the difficulty in measuring the radial velocity field due to its small value compared to its fluctuating value, the radial velocity computations are not taken into account in assessing performance of the velocity models. However, the computational results for the mean radial velocity profiles are plotted in Fig. 4.4. As can be seen in this figure, the computed mean radial velocity profiles match well with the experimental data. Streamlines of non-reacting bluff-body simulations are presented in Fig. 4.7 using various velocity models. It is reported by Dally et al. [6] that the length of recirculation zone is approximately $x/D_b = 1$ or $x = 50$ mm and there is a double-vortex structure attached to the bluff-body. Note that both of the length and the structure of the recirculation zone are well predicted in PDF simulations with the employment of all five velocity models. Overall, the modified LIPM and LSSG models perform better compared to SLM and standard LIPM and LSSG models.

4.2.2 Reacting Bluff-Body Simulations

In this section the performance of velocity models are investigated by performing PDF simulations of reacting bluff-body flow. The profiles of mean axial velocity, the mean radial velocity and the rms fluctuating velocities, the mean mixture fraction and the rms fluctuating mixture fraction are plotted together with the experimental data at axial locations of

$x/D_b = 0.2$, 0.4, 0.8, 1.2, 1.4 and 2.4 in Figs.(4.8)-(4.12). As can be seen in these figures, the main improvement is achieved with standard LIPM, whereas LSSG performs poorly compared to SLM. However the advanced models still perform better in predicting the mean fields in the jet region.

Although the mean radial velocity field is not taken into account in the assessment of velocity models, the radial velocity profiles are plotted in Fig. 4.9. As can be seen in this figure, the shape of radial velocity profiles are captured reasonably well. Another important result is that the mean mixture fraction ration and its variance seem to be insensitive to the velocity models as can be seen in the Fig. 4.12. A similar observation has been also reported by Li et al. [12].

Streamlines of reacting bluff-body simulations are presented in Fig. 4.13 using various velocity models. It is reported by Dally et al. [6] that the length of recirculation zone is approximately $x/D_b = 1.5$ or $x = 75$ mm and there is a double-vortex structure. Note that both the length and the structure of the recirculation zone are well predicted in PDF simulations with the employment of all five velocity models. Overall standard LIPM outperforms compared to other models for reacting bluff-body.

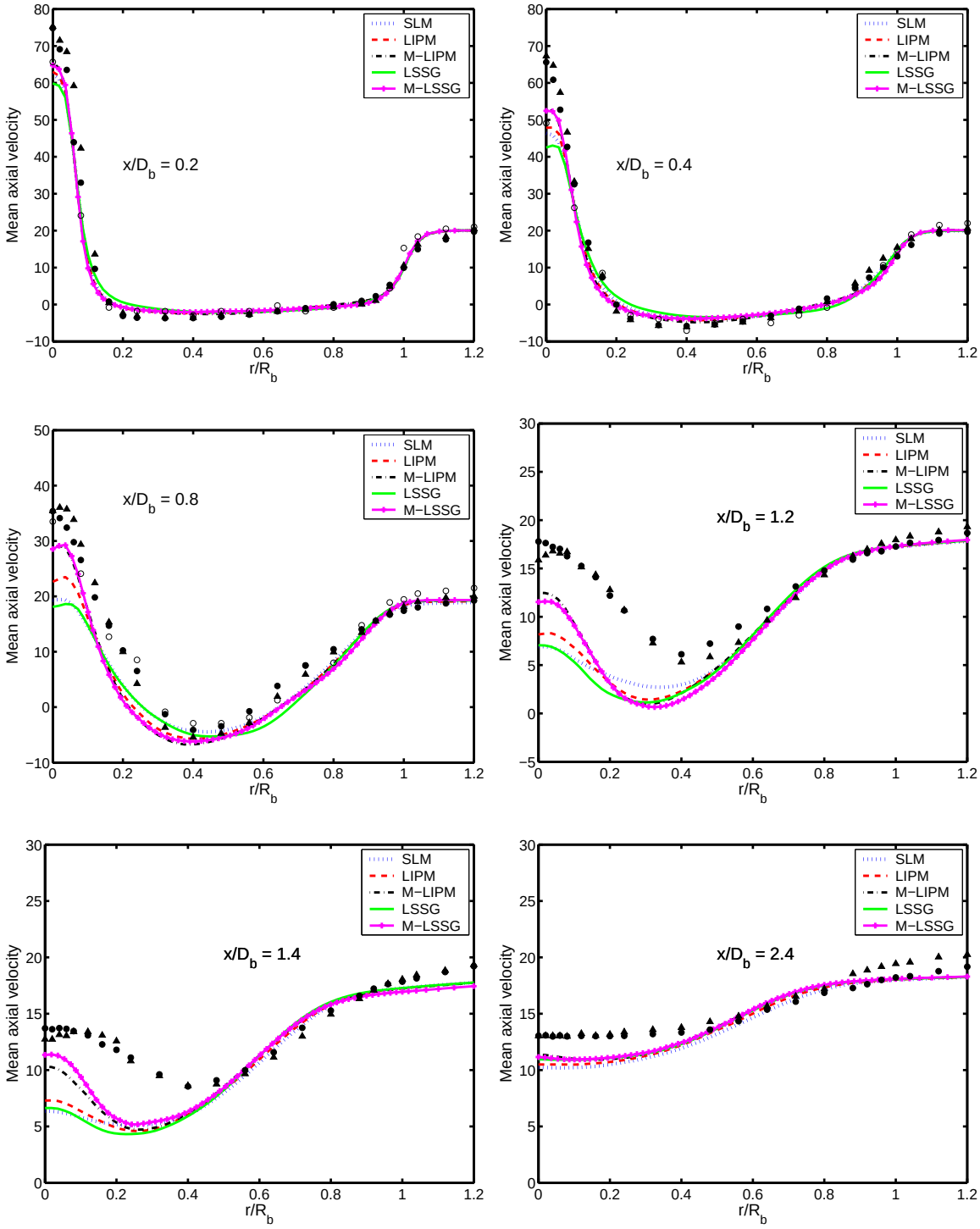

Figure 4.3: Mean axial velocity profiles in non-reacting bluff-body flow using different velocity models. Dotted, dashed, dashed-dotted, solid and dashed lines denote the results obtained with the SLM, the standard LIPM, the modified LIPM, the standard LSSG and the modified LSSG, respectively.

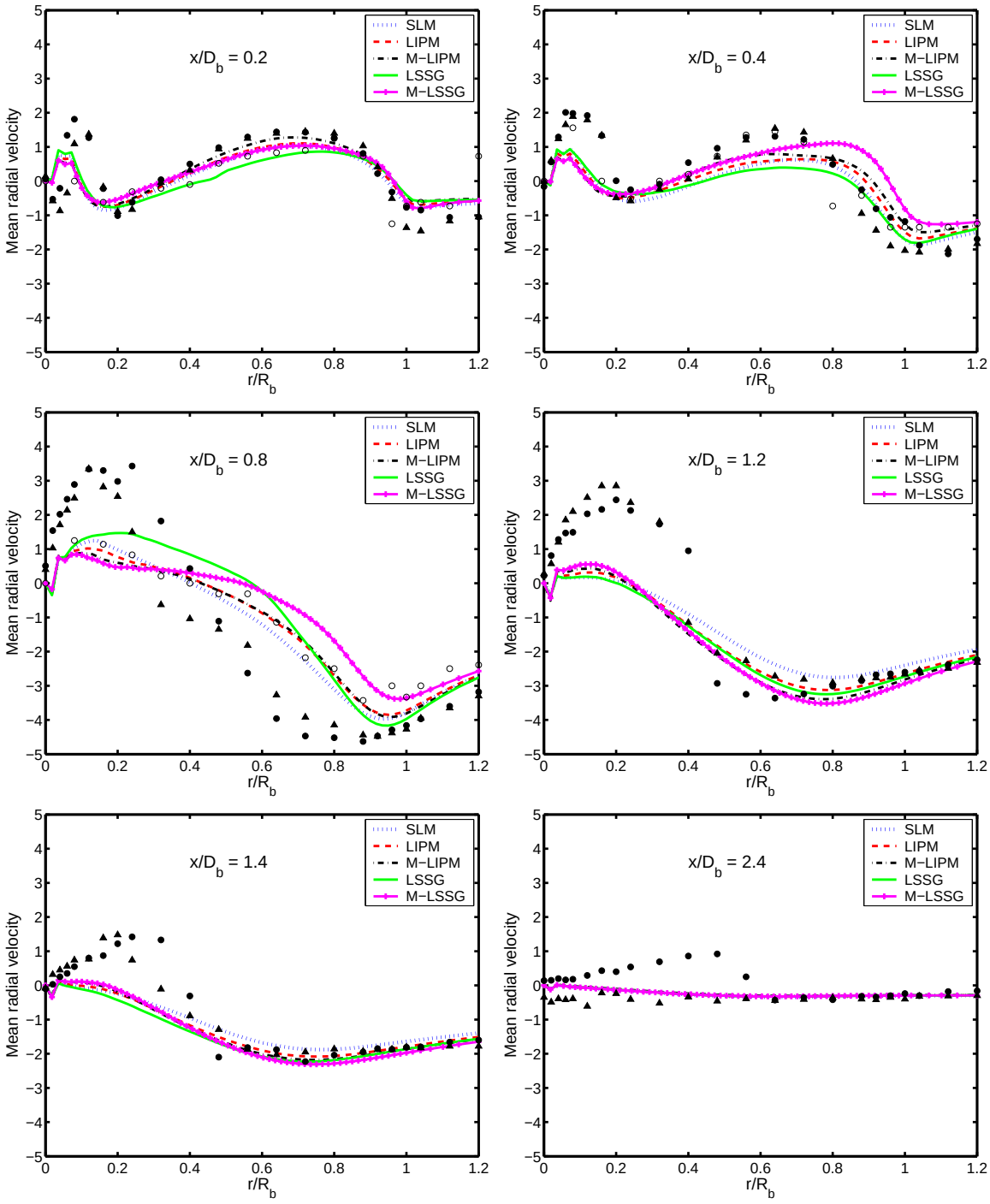

Figure 4.4: Mean radial velocity profiles in non-reacting bluff-body flow using different velocity models. Dotted, dashed, dashed-dotted, solid and dashed lines denote the results obtained with the SLM, the standard LIPM, the modified LIPM, the standard LSSG and the modified LSSG, respectively.

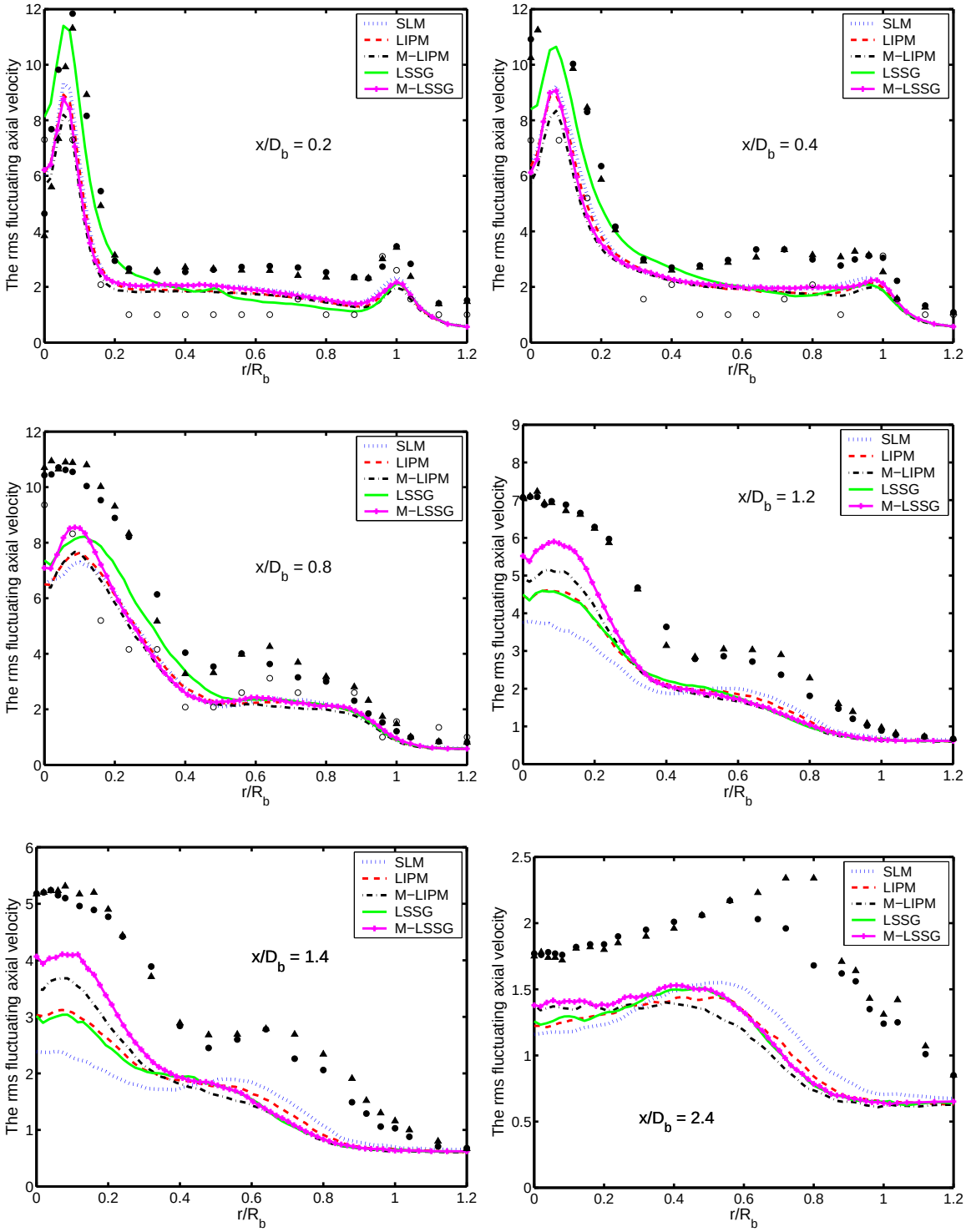

Figure 4.5: Rms axial velocity profiles in reacting bluff-body flow using different velocity models. Dotted, dashed, dashed-dotted, solid and dashed lines denote the results obtained with the SLM, the standard LIPM, the modified LIPM, the standard LSSG and the modified LSSG, respectively.

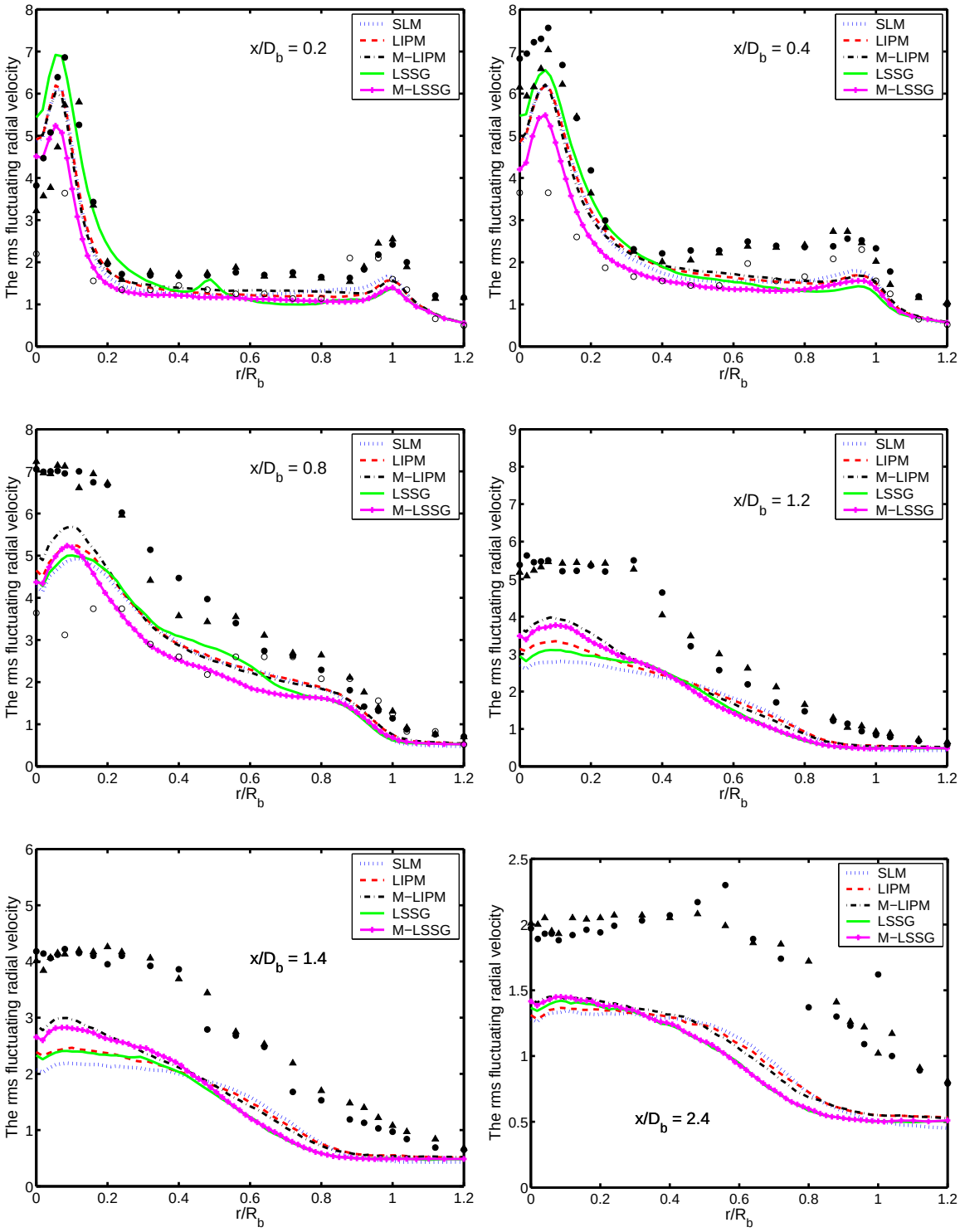

Figure 4.6: Rms radial velocity profiles in non-reacting bluff-body flow using different velocity models. Dotted, dashed, dashed-dotted, solid and dashed lines denote the results obtained with the SLM, the standard LIPM, the modified LIPM, the standard LSSG and the modified LSSG, respectively.

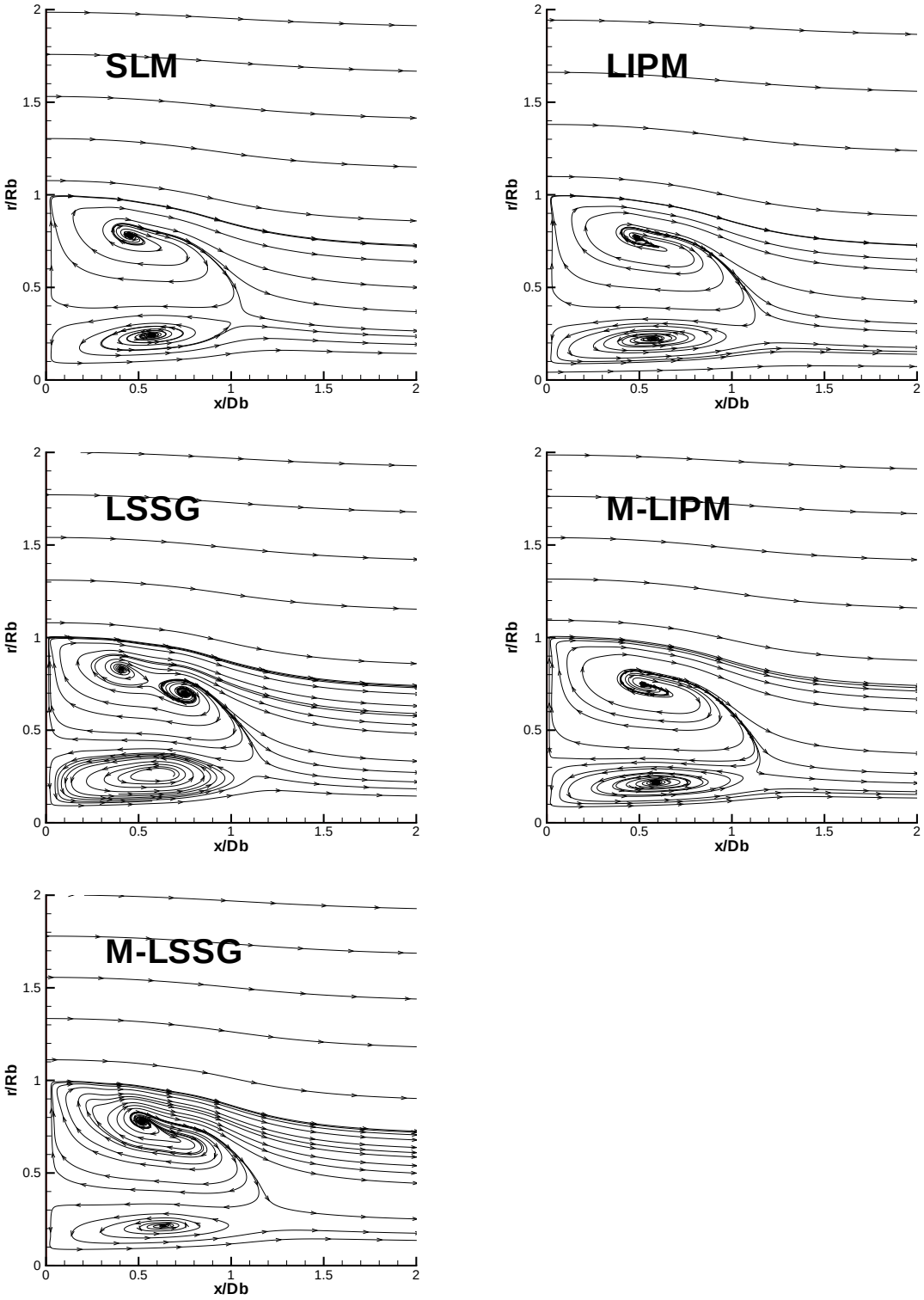

Figure 4.7: Computed streamlines for the non-reacting bluff body flow near the bluff-body.

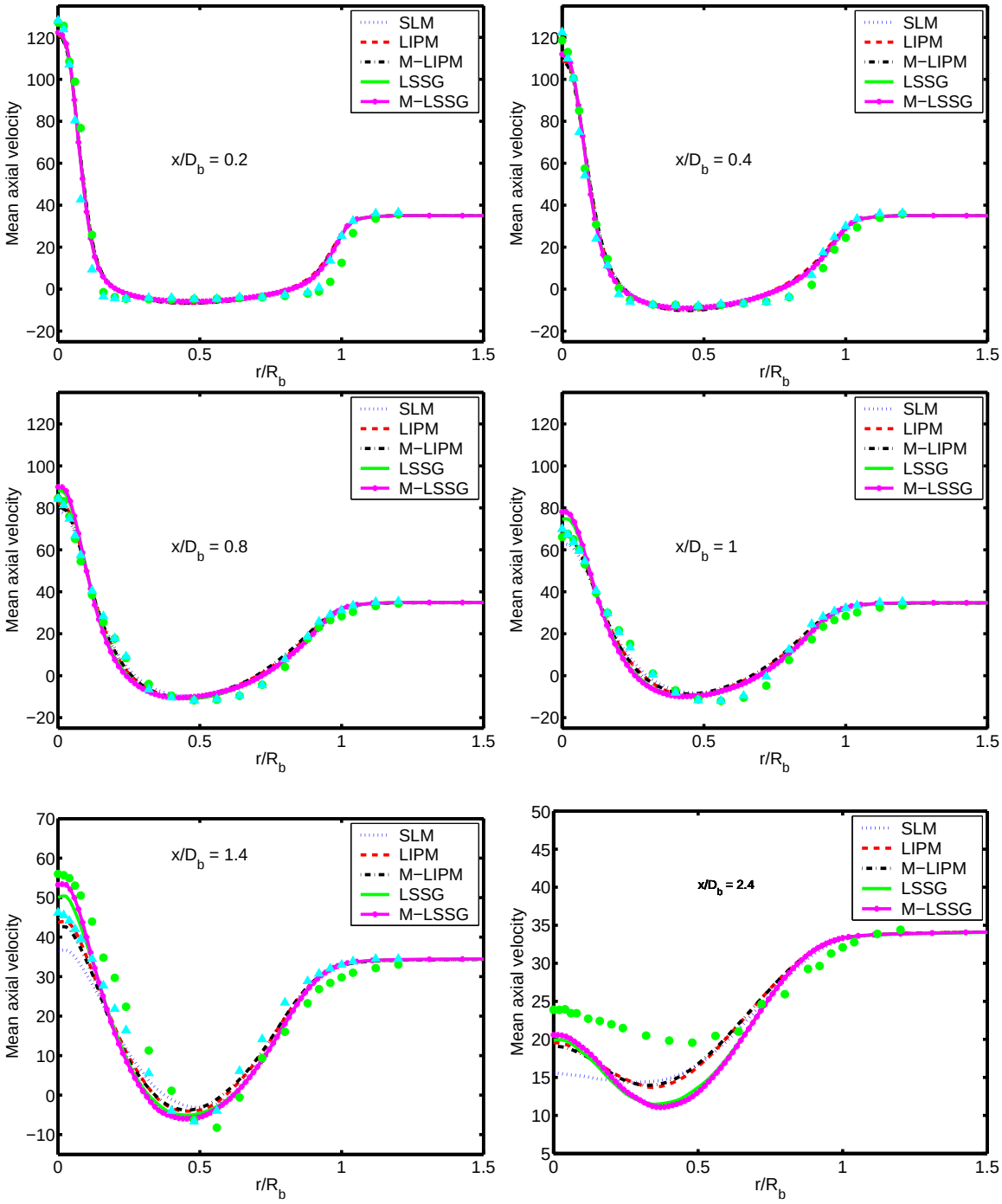

Figure 4.8: Mean axial velocity profiles in reacting bluff-body flow using different velocity models. Dotted, dashed, dashed-dotted, solid and dashed lines denote the results obtained with the SLM, the standard LIPM, the modified LIPM, the standard LSSG and the modified LSSG, respectively.

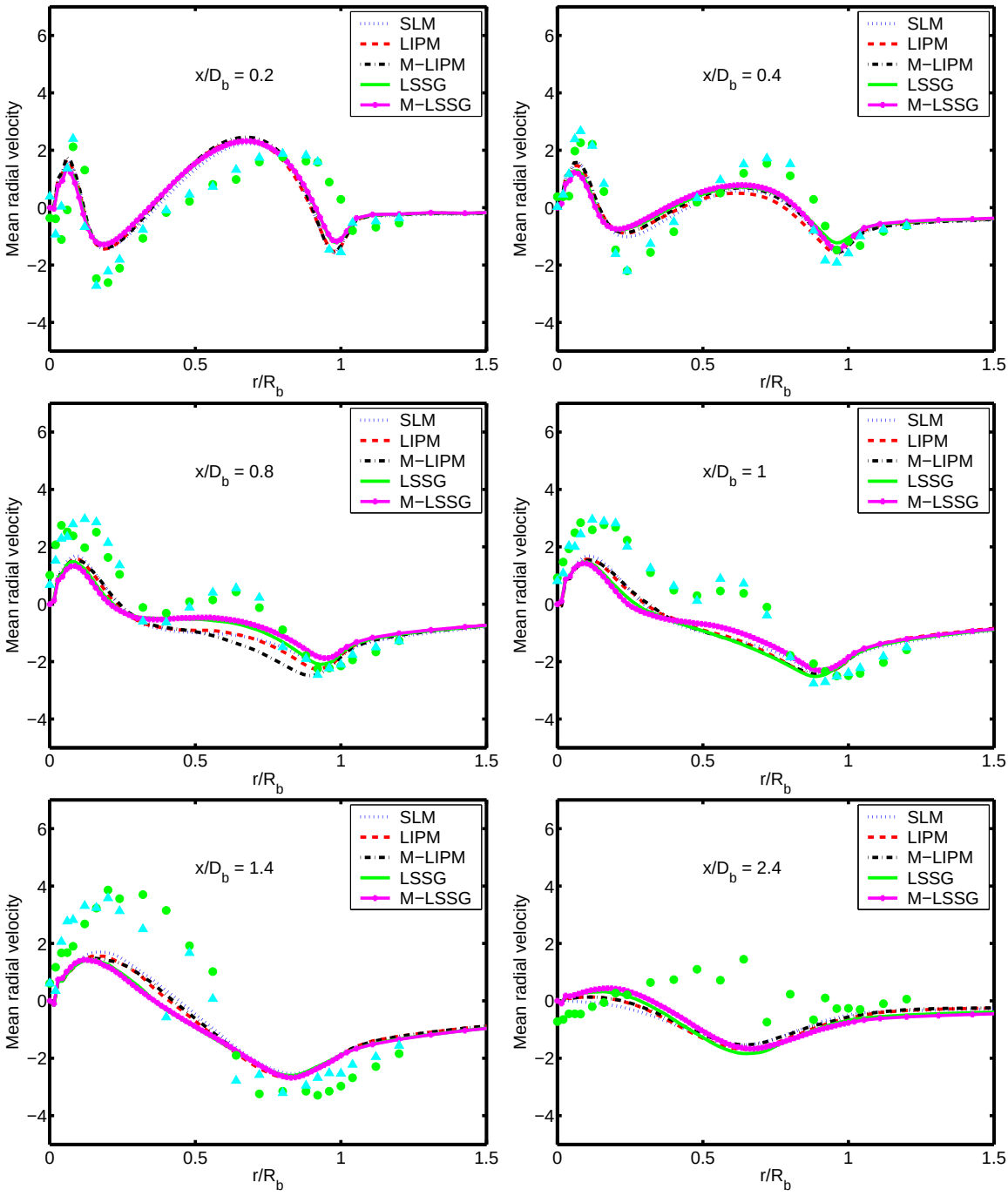

Figure 4.9: Mean radial velocity profiles in reacting bluff-body flow using different velocity models. Dotted, dashed, dashed-dotted, solid and dashed lines denote the results obtained with the SLM, the standard LIPM, the modified LIPM, the standard LSSG and the modified LSSG, respectively.

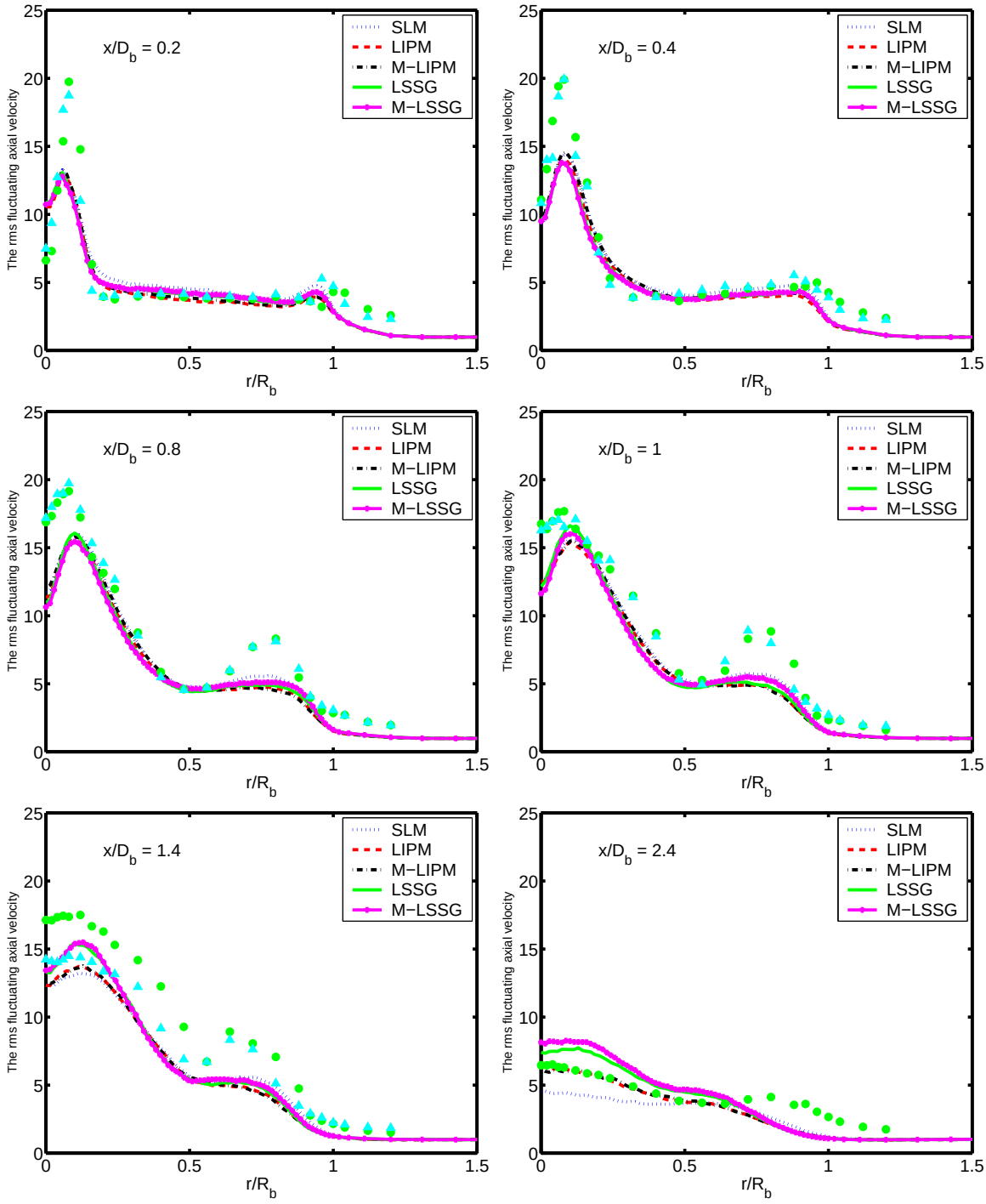

Figure 4.10: Rms axial velocity profiles in reacting bluff-body flow using different velocity models. Dotted, dashed, dashed-dotted, solid and dashed lines denote the results obtained with the SLM, the standard LIPM, the modified LIPM, the standard LSSG and the modified LSSG, respectively.

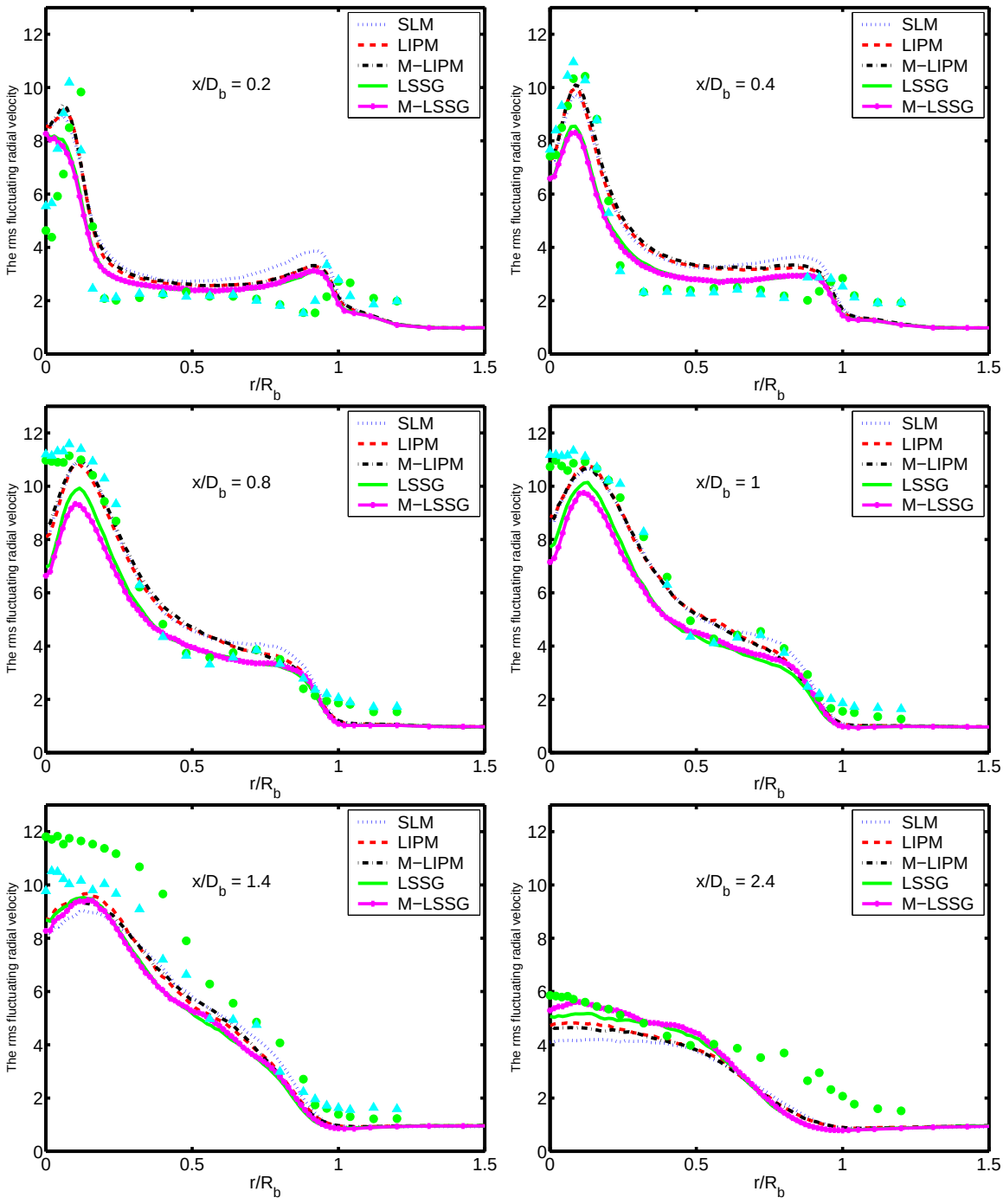

Figure 4.11: Rms radial velocity profiles in reacting bluff-body flow using different velocity models. Dotted, dashed, dashed-dotted, solid and dashed lines denote the results obtained with the SLM, the standard LIPM, the modified LIPM, the standard LSSG and the modified LSSG, respectively.

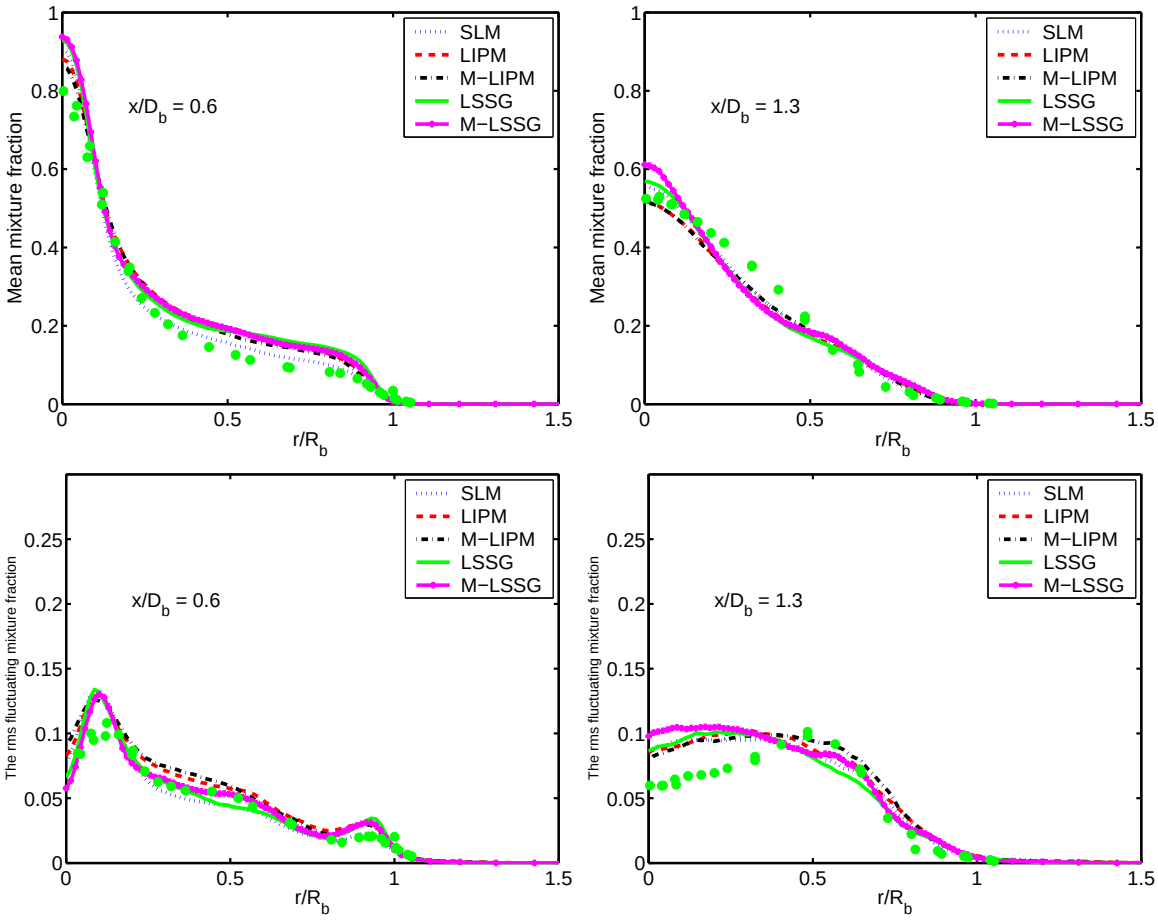

Figure 4.12: Mean mixture fraction and rms fluctuating mixture fractionprofiles in reacting bluff-body flow using different velocity models. Dotted, dashed, dashed-dotted, solid and dashed lines denote the results obtained with the SLM, the standard LIPM, the modified LIPM, the standard LSSG and the modified LSSG, respectively.

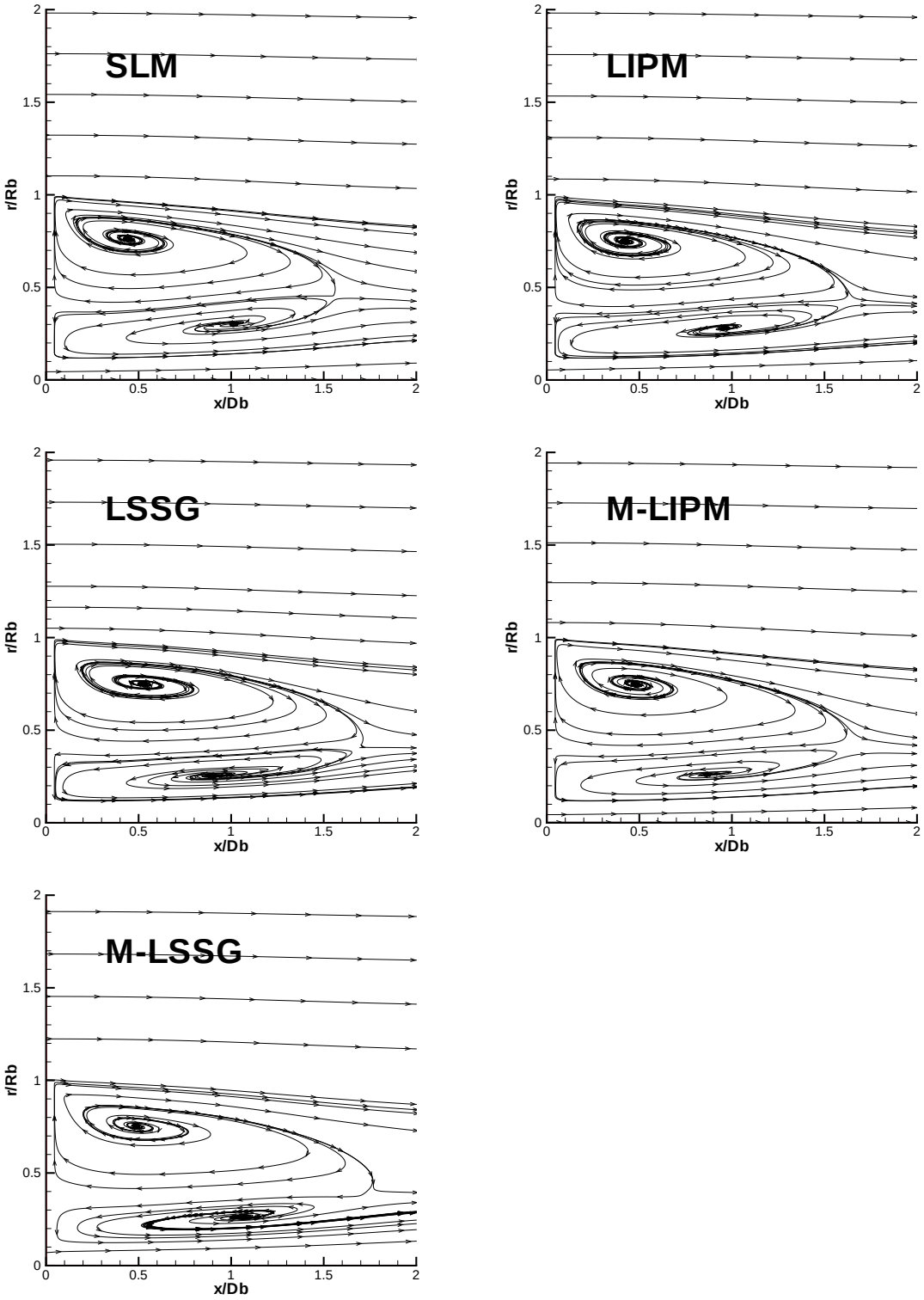

Figure 4.13: Computed streamlines for the reacting bluff body flow near the bluff-body.

Chapter 5

CONCLUSIONS AND COMMENTS

In this thesis PDF simulations of reacting and non-reacting bluff-body flows are performed using a new hybrid FV/particle method with advanced velocity models. Furthermore, performance of velocity models are assessed and a first step toward the optimization of velocity models is taken.

The hybrid method has been successfully applied to the non-reacting and reacting bluff-body flows. The statistical stationarity of the solutions has been demonstrated and it is shown that the method is grid convergent for both reacting and non-reacting bluff-body flows. Stable converged solutions are obtained even on a 128×128 grid, which is in contrast with the earlier PDF computations[10]. A 96×96 grid is found to be sufficient to reduce the spatial error below 5% and so it is used throughout the calculations. In addition, 50 particles per cell are employed in all the calculations since the bias error is virtually eliminated by the consistent hybrid method and statistical error is reduced by time averaging. Time-averaging factors are set to 5, 20, 500 for N_{TA}^{FV}, N_{TA}^{P2FV} and N_{TA}^{P2P}, respectively.

The new hybrid method has been also used to study performance of the PDF velocity models and an attempt has been made towards optimizing the velocity model constants. For this purpose, in addition to the SLM, two other popular velocity models, i.e., Lagrangian Isotropization of Production Model (LIPM) and Lagrangian Speziale Sarkar Gatski Model (LSSG) which are approximately equivalent to IPM of Noat et al. [19] and SSG of Sarkar et al. [27] at the second moment closure level are employed and their performances for the bluff-body flows are evaluated. Due to its simplicity, a flamelet approach is used in the computations. Although the main interest is on the accurate calculations of mean and the rms velocity fields, the sensitivity of the computed results to the model constants for the mixture fraction and the variance of the mixture fraction are also presented. Although mean fields in reacting bluff-body flow are found less sensitive to model constants, it has been found that mean fields are very sensitive in non-reacting bluff-body flow. The assessment is

done by comparing the mean fields with the average of the most recent two experiments of Masri et al. [14]. The accuracy of the prediction of the mean fields is evaluated through the cumulative percentage error for selected flow properties. It has been found that a modified LSSG has the best performance in predicting mean fields of non-reacting bluff-body flow, whereas standard LIPM and LSSG perform better for reacting case. The modification is done by changing C_5 coefficient of LSSG from 0.4 to 0.35 and α_2 coefficient of LIPM from 3.5 to 2.1. With the modification of velocity models significant improvements are achieved in predicting mean fields, where improvements are up to 25%. For both PDF simulations of reacting and non-reacting bluff-body flows SLM has the worst performance in the jet region.

It is found that 20 CPU hours are needed to carry out a PDF simulation for both non-reacting and reacting bluff-body flow simulations on a P-IV PC computer node on Hattusas HPC.

BIBLIOGRAPHY

[1] Commercial cfd software. *http://www.cd-adapco.com*.

[2] Commercial cfd software. *http://www.fluent.com*.

[3] Commercial cfd software. *http://www.ansys.com/products/cfx.asp*.

[4] R. Cao, H. Wang, and S.B. Pope. The effect of mixing models in pdf calculations of piloted jet flames. *31th combustion symposium(accepted)*, 2006.

[5] LS Caretto, AD Gosman, SV Patankar, and DB Spalding. Two calculation procedures for steady, three-dimensional flows with recirculation. *3rd Int Conf on Numerical Methods in Fluid Mechanics*, 1972.

[6] B.B. Dally, D.F. Fletcher, and A.R. Masri. Modelling of turbulent flames stabilised on a bluff-body. *Combust. Theory Modelling*, 2:193–219, 1998.

[7] C. Dopazo. *Recent developments in PDF methods, in: P.A. Libby, F.A. Williams (Eds.), Turbulent Reacting Flows, Academic Press, London, 1994, p.375*, 2003.

[8] T.D. Dreeben and S.B. Pope. Nonparametric estimation of mean fields with application to particle methods for turbulent flows. *Cornell Report FDA 92-13*, 1992.

[9] D.C. Haworth and S.B. Pope. A generalized langevin model for turbulent flows. *Phys. Fluids*, 29:387–405, 1986.

[10] P. Jenny, M. Muradoglu, K.Liu, S.B. Pope, and D.A. Caughey. Pdf simulations of a bluff-body stabilized flow. *J. Comp. Phys.*, 169:1–23, 2001.

[11] P. Jenny, S.B. Pope, M. Muradoglu, and D.A. Caughey. A hybrid algorithm for the joint pdf equation of. turbulent reactive flows. *J. Comp. Phys.*, 166:218–252, 2001.

[12] G. Li, B. Naud, and D. Roekaerts. Numerical investigation of a bluff-body stabilised nonpremixed flame with different reynolds-stress models. *Flow, Turbulence and Combustion*, 70:211–240, 2003.

[13] K. Liu, S.B Pope, and D Caughey. Calculations of bluff-body stabilized flames using a joint pdf model with detailed chemistry. *Combustion and Flame*, 141:89–117, 2005.

[14] A.R. Masri. *Tech. Report, available at: http://www.mech.eng.usyd.au/research/energy.*

[15] M. Muradoglu, K.Liu, and S.B. Pope. Pdf modeling of a bluff-body stabilized turbulent flame. *Combust. Flame*, 132:115–137, 2003.

[16] M. Muradoglu, S.B. Pope P. Jenny, and D.A. Caughey. A consistent hybrid finite-volume/particle method for the pdf equations of turbulent reactive flows. *J. Comp. Phys.*, 154:342–371, 1999.

[17] M. Muradoglu and S. B. Pope. Local time-stepping algorithm for solving the probability density function turbulence model equations. *AIAA J.*, 40:1755–1763, 2002.

[18] M. Muradoglu, S.B. Pope, and D.A. Caughey. The hybrid method for the pdf equations of turbulent reactive flows: consistency conditions and correction algorithms. *J. Comp. Phys.*, 172:841–878, 2001.

[19] D. Naot, A. Shavit, and M. Wolfstein. Interaction between components of the turbulent velocity correlation tensor. *Isr. J. Tech.*, 8:259–269, 1970.

[20] M. Peric and J.H. Ferziger. *Computational Methods for Fluid Dynamics*, 1996.

[21] S. B. Pope. Pdf methods for turbulent reactive flows. *Prog. Energy Combust Sci.*, 11:119–192, 1985.

[22] S.B. Pope. On the relationship between stochastic lagrangian models of turbulence and second-moment closures. *Phys. Fluids*, 6:973–985, 1986.

[23] S.B. Pope. *PDF2DV: A Fortran code to solve the modelled joint PDF equations for two-dimensional recirculating zones. Unpublished work*, 1994.

[24] S.B. Pope. *Turbulent Flows*, 2000.

[25] J. Rotta. Statistische theorie nichthomogener turbulenz. *Z. Phys.*, 129:547–572, 1951.

[26] P.R. Van Slooten, Jayesh, and S.B. Pope. Advances in pdf modeling for inhomogeneous turbulent flows. *Phys. Fluids*, 10:246–265, 1998.

[27] C.G. Speziale, S.Sarkar, and T.B. Gatski. Modeling the pressure-strain correlation of turbulence: an invariant dynamical systems approach. *J. Fluid Mech.*, 227:245–272, 1991.

[28] Q. Tang, J. Xu, and S.B. Pope. Pdf calculations of local extinction and no production in piloted-jet turbulent methane/air flames. *Proceedings of the Combustion Institute*, 28:133–139, 2000.

[29] TNF web site. *http://www.ca.sandia.gov/TNF*.

[30] J. Xu and S.B. Pope. Pdf calculations of turbulent nonpremixed flames with local extinction. *Combustion and Flame*, 123:281–307, 2000.

VITA

Özkan Eren was born in Bursa, Turkey on February 16, 1981. He received the B.S. degree in Civil Engineering from Boğaziçi University, Istanbul, in 2004. In October 2004, he joined to the Computational Science and Engineering Department of Koç University, Istanbul, Turkey as a teaching and research assistant and worked on *"PDF modeling of the bluff-body stabilized turbulent reactive flows."*